NUMERICAL AND EXPERIMENTAL INVESTIGATION OF AN ELECTRIC VEHICLE BATTERY MODULE THERMAL MANAGEMENT SYSTEM

A Thesis Submitted to
the Graduate School of
İzmir Institute of Technology
in Partial Fulfillment of the Requirements for Degree of

MASTER OF SCIENCE

in Mechanical Engineering

by
Çağlar GEDİKSİZ

June 2022
İZMİR

ACKNOWLEDGMENTS

ABSTRACT

NUMERICAL AND EXPERIMENTAL INVESTIGATION OF AN ELECTRIC VEHICLE BATTERY MODULE THERMAL MANAGEMENT SYSTEM

It is vital to develop battery technology in electric vehicles. The biggest problem experienced is the thermal runaways, which is a phenomenon that may cause burning and explosions following the decrease in battery capacities. The thermal runaway problem can be solved by using the thermal management system to keep the temperature range under control. In this study, a 6.7kWh battery pack was produced. Battery pack operation consists of two parts, mechanical and thermal. In the mechanical part, battery pack assembly and drop tests were carried out. Besides, a numerical and experimental study supported drop tests. As a result of this study, the battery case did not show permanent deformation as suggested in the numerical experiments. Discharge characteristics and battery module model were discussed in the thermal management part. The gap between the battery cells reached its most efficient value at 8 mm. In the developed battery module, thermal management was attempted using a heat plate and a cooling pipe. According to the numerical results, the battery module reaches 311.37K at 10C discharge. In the experimental process, the battery pack was charged with 15A and discharged with 30A. Moreover, the temperature values reached a maximum of 31 degrees. In the experiment on electric vehicles, a maximum discharge level of 255A was observed. In this experiment, the battery pack reached a maximum of 36 degrees.

Keywords: Battery Thermal Management, NTGK Model, Forced Convection, Battery Pack Manufacture, Drop Test

ÖZET

BİR ELEKTRİKLİ ARAÇ BATARYA MODÜLÜ ISIL YÖNETİM SİSTEMİNİN SAYISAL VE DENEYSEL OLARAK İNCELENMESİ

Elektrikli araçlarda pil teknolojisinin geliştirilmesi hayati önem taşımaktadır. Yaşanılan en büyük sorun, pil kapasitelerinin düşmesini takiben yanma ve patlamalara neden olabilen bir olgu olan termal kaçaklardır. Termal kaçak sorunu, sıcaklık aralığını kontrol altında tutmak için termal yönetim sistemi kullanılarak çözülebilir. Bu çalışmada 6,7 kWh pil takımı üretilmiştir. Batarya paketi çalışması mekanik ve termal olmak üzere iki kısımdan oluşur. Mekanik kısımda ise pil takımı montajı ve düşürme testleri yapılmıştır. Bunun yanısıra, sayısal ve deneysel bir çalışma, düşürme testlerini destekledi. Bu çalışma sonucunda pil kutusu sayısal deneylerde önerildiği gibi kalıcı deformasyon göstermedi. Termal yönetim bölümünde deşarj özellikleri ve pil modülü modeli tartışıldı. Pil hücreleri arasındaki boşluk 8 mm'de en verimli değerine ulaştı. Geliştirilen pil modülünde bir ısı plakası ve bir soğutma borusu kullanılarak termal yönetim denenmiştir. Sayısal sonuçlara göre pil modülü 10C deşarjda 311,37K değerine ulaşıyor. Deneysel süreçte batarya paketi 15 amper ile şarj edilmiş ve 30 amper ile deşarj edilmiştir. Ve sıcaklık değerleri maksimum 31 dereceye ulaşmıştır. Elektrikli araçlar üzerinde yapılan deneyde maksimum 255 A deşarj seviyesi gözlemlendi. Bu deneyde, batarya paketi maksimum 36 dereceye ulaştı.

Anahtar Kelimeler: Batarya Termal Yönetimi, NTGK Model, Zorlanmış Taşınım, Batarya Paketi Üretimi, Düşürme Testi

TABLE OF CONTENTS

LIST OF FIGURES

Figure   **Page**

LIST OF TABLE

LIST OF SYMBOLS

$\bar{p}$	Average pressure	Pa
Q_{nom}	Total electric capacity	Ah
Q_{ref}	Reference capacity	Ah
$\bar{T}$	Average temperature	K
T_{ref}	Reference temperature	K
c_P	Specific heat capacity	J/(kg K)
$\dot{m}$	Mass flow rate	kg/s
$\dot{q}$	Heat generation rate	W
$\bar{U}$	Average velocity component in each direction	m/s
H_{in}	Height of inlet region	mm
H_{out}	Height of outlet region	mm
j_{ECh}	Volumetric current transfer rate	
j_{short}	Current transfer rate	
k	Turbulent kinetic energy	m^2/s^2
L_{in}	Length of the inlet region	mm
L_{out}	Length of the outlet region	mm
P	Pressure	Pa
t	Time	s
T	Temperature	K
U'	Fluctuations of velocity in each direction	m/s
U	Velocity vector	m/s
W_{in}	Width of the inlet region	mm
W_{out}	Width of the outlet region	mm
SoC	State of charge	
Vol	Volume of the active zone	
x	Component of the energy dissipation rate	m
ΔT	Temperature difference	K
ε	Turbulent kinetic energy dissipation rate	m^2/s^3
ρ	Density	

μ	Viscosity	Pa s
σ_k	Turbulent Prandtl number for k	
σ_ε	Turbulent Prandtl number for ε	
σ_{cp}	Turbulent Prandtl number for based on specific heat at constant pressure	
σ_+	Effective electric conductivity for the positive electrodes	
σ_-	Effective electric conductivity for the negative electrodes	
φ_+	Phase potential of positive electrodes	
φ_-	Phase potential of negative electrodes	
λ	Conductivity	$W/(m^2K)$

CHAPTER 1

INTRODUCTION AND FUNDAMENTALS

Although greenhouse gas problems caused by the combustion of fossil fuels, CO and NOX problems, environmental pollution, climate warming, and energy shortages draw significant attention, the transportation sector has continued to contribute significantly to pollution in terms of fossil fuel use. The tremendous impact of fossil fuels on environmental pollution and global warming made the automotive industry tend to find alternative solutions. Consequently, during last decades, the prohibition of gasoline-powered vehicles has been announced by many governments in order to prevent this pollution (Miele et al. 2020; Shen and Gao 2020). Besides, this policy aims to offer an alternative transportation way to consumers and draw their attention to choosing clean and environmentally friendly sources. Therefore, electric vehicles have been becoming a great opportunity to decarbonize, and reduce dependence on fossil fuels. In terms of sustainability, zero emissions, and cost, EVs completely meet the demands of the automotive industry (Mossali et al. 2020; Rezvani, Jansson, and Bodin 2015; Santos 2017). Government support for the common usage of EVs is dramatically increasing, and the motivations of the community toward EVs are changing positively. The UK aims to become a zero-emission country by 2050. Moreover, China, Norway, Japan, Sweden, Denmark, and India provide significant financial supports for EVs. In the light of these incentives and technology developments, EVs manufacturers reached a sales value of 2.1 million in 2019. According to Jato data, 3.5 and 4.4 million EVs were sold in 2020 and 2021, respectively (Thøgersen and Ebsen 2019; Mossali et al. 2020).

The crucial components of EVs, such as high energy, power density, long cycle life, low self-discharge, fast charging capacity, and efficiency of rechargeable batteries, put the lithium-ion batteries on the frontline in the EVs industry. Besides, the popularity of lithium-ion batteries originated from cost-effectiveness, and the growing number of charging stations, also.

Except for lithium-ion, there are many negative factors such as operating temperature sensitivity and memory effect in Lithium-based batteries and other battery

groups. Therefore, manufacturers prefer lithium-ion battery packs in EVs originating from lithium potential ("The Global Electric Car Sales 2021 in Numbers - JATO" n.d.).

The EVs are investigated in the early 1830s. Surprisingly, many EV applications were made, and EVs became popular. These applications were observed broadly, from tricycles to battery technology and tram development. Then, The USA made an impactful decision to own more than 30.000 EVs. It is known that various battery types, namely non-rechargeable batteries, lead-acid, iron-nickel, nickel-metal hydride, and nickel-cadmium batteries, took part in all these processes. Unfortunately, technical constraints, widely known as battery volume charging time, ambient temperature, and the rapid development of internal combustion engines, and oil resources, made EVs unfavorable. EV Technology has great power to provide energy-saving, sustainable development, national security, and to eliminate oil crisis and environmental issues (Fuqiang et al. 2019; Nitta et al. n.d.).

Hybrid electric vehicles (HEV), battery electric vehicles (BEV), and fuel cell electric vehicles (FCEV) dominate in the EV literature. Basically, the vehicles are composed of 3 parts: power supplies, engines and electronic control systems. Specifically, power supplies divided into 5 major parts namely lithium-ion batteries, nickel-metal hybrid batteries, fuel cells, lead-acid batteries and supercapacitors (Jaguemont, Boulon, and Dubé 2016; Aneke and Wang 2016).

In terms of technical information, lithium-ion batteries reach their maximum potential at room temperature. Besides, high specific energy, high energy density, cycle life, low self-discharge and long shelf life are among positive characteristics of lithium-ion batteries. On the other hand, the most remarkable negative property is that keeping the lithium-ion batteries within the operating temperature range is necessary. Therefore, the development of the battery thermal management system plays a crucial role in the development of lithium-ion batteries (Basu et al. 2016; Zhang et al. 2014).

Cells come together to form modules and then packages. Voltage and capacity in packages are obtained with serial and parallel configurations. The SoC-SoH in the cells varies according to the connection type, contact area, and contact resistances. Therefore, uneven current flow and heat generation trigger an increase in temperature followed by thermal runaways. Thus electric heating, air heating/cooling, liquid heating/cooling, and PCM heating/cooling are the focus for BTMS (C.-K. Huang et al. 2000; Roe et al. 2022). As the Table 1 shows, there are many causes of major lithium-ion battery accidents such as mechanical, electronic and thermal faults. Basically, mechanical faults can be

classified as mechanical shock, drop, penetration, crash/crush, rollover, vibration, immersion. Flammability and emission are examples of the chemical faults. Further, electrical faults are divided into 3 parts namely overcharge/over-discharge, internal short circuit, and external short circuit. Lastly, thermal faults; thermal stability, extreme cold temperature, overheat, thermal shock and cycling (Y. Wang et al. 2018; Zolot, Pesaran, and Mihalic 2002; "10.1115/IECEC2001-ET-07 " 2013; Sun et al. 2020; "(4) (PDF) Thermal Evaluation of the Honda Insight Battery Pack" n.d.). (Table 1)

Table 1. Selected accidents of the li-ion battery in last ten years.
(Source: Feng et al. 2018)

Year	Loc.	Accident	Year	Loc.	Accident
2008	Us	Fire accident in Li-ion battery pack of modified Prius caught fire on highway	2015	Us	Nissan Leaf got destroyed on the road due to fire
2011	Us	A Chevy Volt got burnt three weeks after a side pole impact test	2016	Norway	During fast-charging, a Tesla Model S got burnt
2012	China	A BYD E6 taxi caught fire after hitting a tree due to a collision with a Nissan GTR	2016	China	Fire accident leads to the burning of Wuzhou Dragon EV bus
2013	Us	The fire triggered in the APU battery module	2016	China	An iEV5 caught fire
2013	Japan	The fire triggered in the battery module in a Boeing 787 flight	2016	Italy	On the road, an EV police car caught fire
2013	Us	Two Tesla Model S caught fire on the highway after running over a large metal object	2017	Germany	VW e-Golf got fire
2015	China	During charging, a Wuzhou Dragon EV bus got fire and started burning	2018	Switzerland	Following a crash, the Tesla battery reignited again
2015	China	The Hybrid EV bus battery module started burning	2019	England	Complete burning of Tesla Model X from 2017

CHAPTER 2

LITERATURE REVIEW

Lithium-ion and Ni-MH battery packs are competing in the market. 250Ah prismatic cells and 6Ah HEV battery modules are commercially produced in-house Ni-MH. Toyota decided to switch to the Ni-MH battery pack in 2015. Moreover, Fitch says the market share for NMC batteries will increase by 63%. The Democratic Republic of Congo has cobalt raw material but cobalt prices are unstable due to political unrest.

Furthermore, lithium-ion batteries technology has been tried to develop new cathodes to reduce their dependence on cobalt. Tesla wants to develop NCA cylindrical batteries and integrates them with BMS to form battery packs. Battery specifications of some EVs are given in Table 3. Battery selection depends on capacity, quality, safety and cost (G. Zhao, Wang, and Negnevitsky 2022).

Table 2. List of commercial EV used air-cooled BTMS.
(Source: Sharma and Prabhakar, 2021)

Year	Make	Model	kWh	EV type	Year	Make	Model	kWh	EV type
2009	Nissan	Leaf BEV	24	Pure	2016	JAC	iEV5	23	Pure
2010	Honda	Insight	20	Pure	2017	Toyota	Prius Prime	8.8	Plug-in
2010	Mitsubishi	i-MiEV	16	Pure	2017	VW	e-Golf	32	Pure
2012	Nissan	e-NV200	45	Pure	2019	Renault	Zoe	52	Pure
2016	Reynolds	ZOE EV	45.6	Pure	2019	Nissan	Leaf	40	Pure
2016	Hyundai	IONIQ	28	Pure					

Honda Insight and Toyota Prius were the first commercially available hybrid electric vehicle to use air cooling strategies for BTMS. The battery pack of the Honda Insight contains 20 modules of cylindrical batteries, each of 144 V, 0.94 kWh, whereas the Toyota Prius pack consist of 38 modules of prismatic cells, each of 273.6 V and 1.78 kWh capacity. The battery pack of both EVs were cooled using conditioned air taken

from the cabinet, and the absorbed heat released into the environment. Air-cooled BTMS has been used in many other EVs such as Nissan Leaf, Mitsubishi i-MiEV, Reynolds ZOE EV, and Renault Zoe (Sharma and Prabhakar 2021). (Table 2)

Table 3. Specifications of some power batteries on hot-sale EVs
(Source: G. Zhao, Wang, and Negnevitsky 2022)

Type	Bat. Man.	EV Model	Capacity (kWh)	Nominal Driving Range
NA	Panasonic	Tesla Model S75D	75	405
		Tesla Model S90D	90	445
		Tesla Model S100D	102	510
		Tesla Model SP100D	102	505
LCO	Panasonic, CATL	Tesla Roadster(2020)	200	1000
		Daimler Benz Smart	18	120
		Fortwo Electric Drive		
LFP	BYD,GS Yuasa, Lishem, Valence	BYD E6	82	390
		Mitsubishi iMiEV	16	95
NMC	CATL, Hitachi, LG Chem, Samsung SDI, Panasonic, SK innovation	Chevrolet Bolts EV	60	350
		Chevrolet Volts	18.4	85
		Ford Focus Electric	33.5	180
		BYD E6	82	390
		Roewe Ei5	52.5	301
		Renault Zoe ZE50 R135	41	230
		Nissan LEAF	30	170
		NIO ES6	70	415
		BMW i3	33	180

2.1. Air Cooling

Temperature homogeneity and energy consumption issues are essential for air cooling design. It is the notion that the cells' spacing, the module housing, and the inlet and outlet position are essential parameters for prismatic lithium-ion. On the other hand, the arrangement is essential in cylindrical cells than in prismatic cells. Lithium-ion packages are available in aligned, staggered, and cross designs. Chen et al. developed the air cooling system using the Z-type manifold. In the numerical study, the maximum temperature was 47.3 °C after the prismatic batteries had been loaded at 5C. The temperature difference was 10.3 °C (K. Chen, Chen, et al. 2018). They reduced the cell spacing and the highest temperature value by 60 % by optimizing using the Z manifold. Likewise, they developed the optimization algorithm on the U manifold and investigated the gap value in the system. The maximum temperature was 43.4 °C after the prismatic batteries were loaded at 5C. The temperature difference was identified as 5.6 °C. This design managed to reduce power consumption by 50 % (K. Chen, Song, et al. 2018).
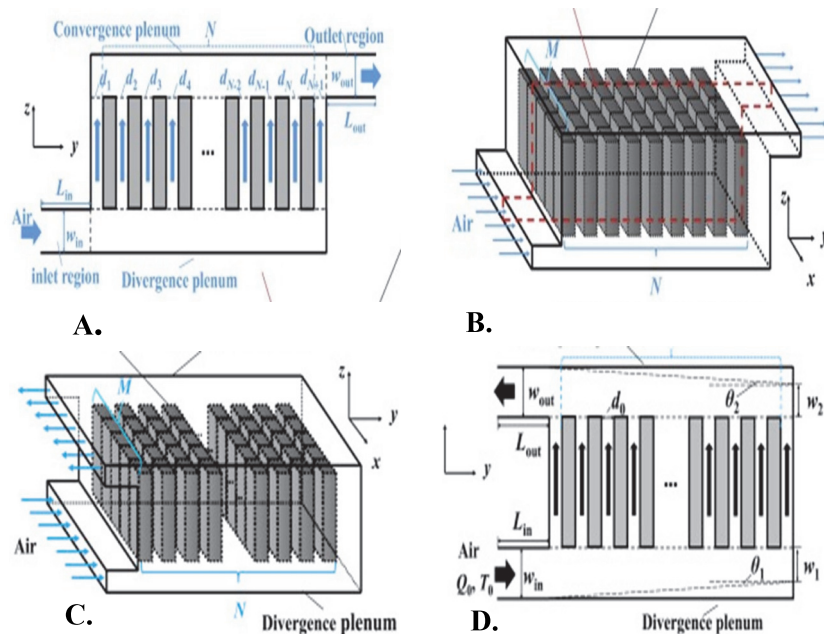
Figure 1. (A) Two-dimensional (B) Three-dimensional BTMS (Source: K. Chen, Chen, et al. 2018) (C) Three-dimensional (D) Two-dimensional BTMS (Source: K. Chen, Song, et al. 2018)

In the experimental study, Kokam SLPB75106100 was studied with lithium-ion. In this study, 25 °C and 40 °C were chosen as ambient temperatures. Gungor et al. found that the maximum temperature difference on the battery surface of 11° at 3C discharge and 17° at 5C (discharge rate). Ventilation and low ambient temperature reduced by 3% battery capacity (Gungor, Cetkin, and Lorente 2022b). The Z manifold was used in the experimental and theoretical study on the 15S1P battery pack. Gocmen et al. optimized the battery positions and documented that the maximum temperature difference decreased from 12K to 0.3K (Gocmen and Cetkin 2022).
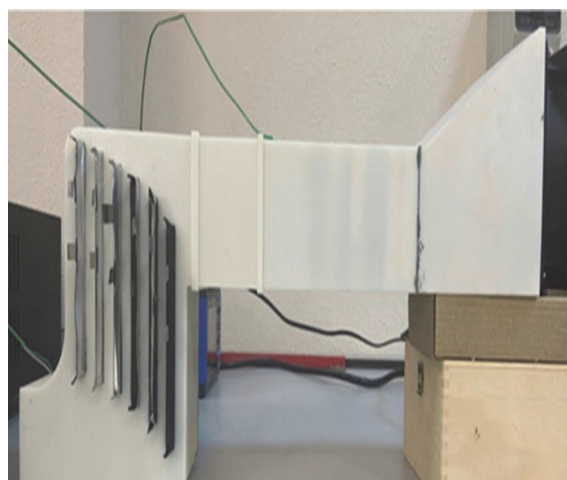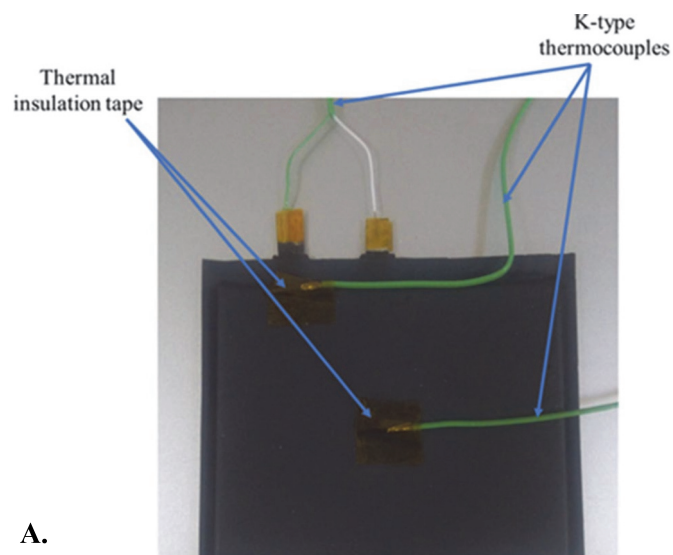
Figure 2. (A) Thermocouple locations on the Lithium-ion battery cell (Source: Gungor, Cetkin, and Lorente 2022b) . (B) Experimental setup (Source: Gocmen and Cetkin 2022)

For the battery module gap values, Kirad et al. proposed that the longitudinal and transverse distances between the batteries make a difference in cooling efficiency and affect temperature homogeneity. After the 18650 lithium-ion battery was loaded at 2C, the temperature difference was 2.5 °C (Kirad and Chaudhari 2021). Fan et al., who conducted an experimental study with 32 cylindrical lithium-ion cells, studied at 1C and 2C. They proved that the aligned arrangement has better temperature and cooling performance than the others. The temperature was decreased by 12 % when compared to the cross arrangement. The desired temperature homogeneity could not be achieved in staggering and cross-arrangement (Fan et al. 2019).
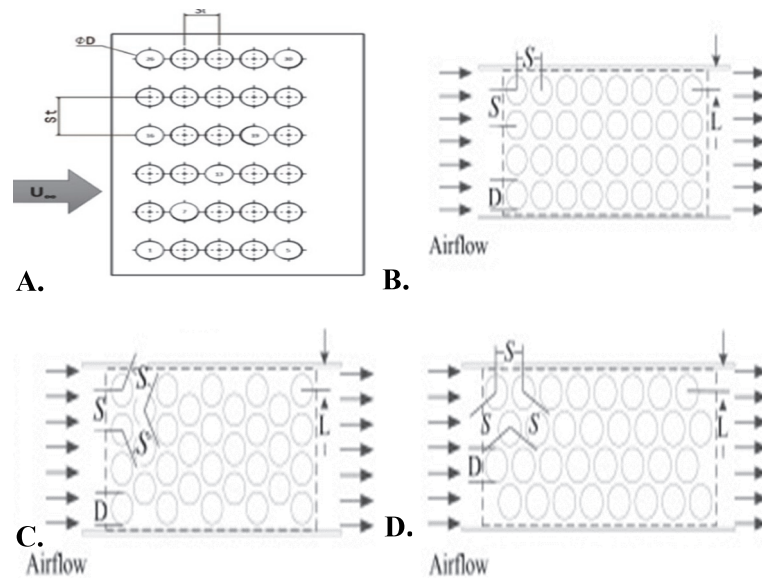
Figure 3. (A) Aligned arrangement (Source: Kirad and Chaudhari 2021) (B) Aligned arrangement (C) Staggered arrangement (D) Cross arrangement (Source: Fan et al. 2019)

Lu et al. studied the cooling duct and air supply of a stepwise designed model. They performed air inlet and outlet from different points. The highest yield was obtained when the inlet and outlet designs were placed at the top and bottom of the battery pack, respectively. In the numerical study with 18650 lithium-ion batteries, a maximum temperature of 29.45 °C was obtained at 0.5C (Lu et al. 2018). Furthermore, Wang et al. designed a fan battery model and indicated that putting a fan on the battery module gives better performance in terms of cooling. A maximum temperature of 33.59 °C was

achieved at 3C with Sanyo 18650 lithium-ion batteries. Furthermore, the temperature difference was 2.95 °C (T. Wang et al. 2014).
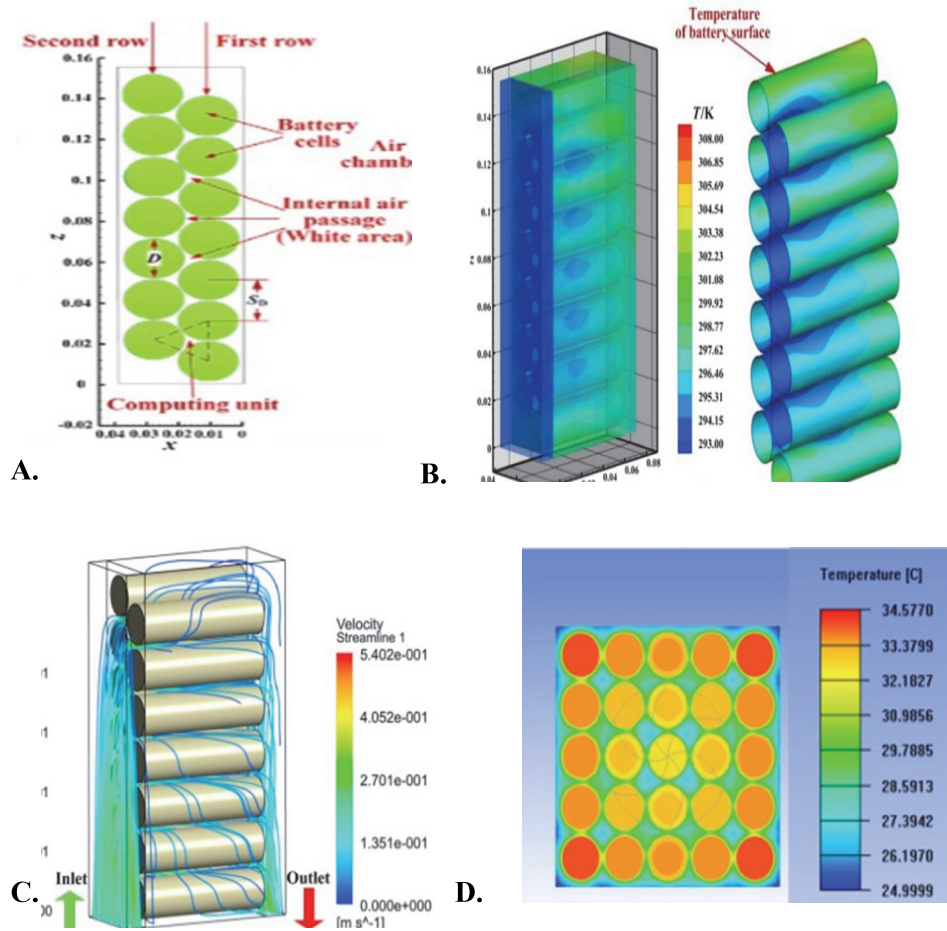
Figure 4. (A) Internal air coolant passage. (B) Temperature fields of the stagger-arranged battery packs. (C) Streamlines of the stagger-arranged battery packs (Source: Lu et al. 2018). (D) Temperature of 3 × 8 battery module without airflow (Source: T. Wang et al. 2014).

Peng et al. achieved a realistic approach by re-modeling the temperature inconsistency of the cells in the battery pack for a 1C discharge rate. They suggested a model with the inlet and outlet on the same side (Peng et al. 2019). Ji et al. proved that changing the distance between cells positively affects temperature homogeneity (Ji et al. 2019). Li et al. proposed an optimization method for reducing volume and increasing the performance of an air cooling system. When the MOGA algorithm was used, the battery pack demonstrated a higher thermal performance. The maximum temperature was 34.5

°C at 2C, and the temperature difference was 3.1 °C (W. Li et al. 2019). Zhou et al. have succeeded in reducing the temperature by 20 °C using an air distribution pipe for cylindrical lithium-ion batteries. After loading 18650 batteries at 5C, the temperature increased to 37.85 °C.

Furthermore, they found a temperature difference of 5.5 °C (Zhou, Xu, et al., 2019). Jiaqiang et al. placed different inlets and outlets on the battery container. They obtained improved cooling performance by using lateral inlet and outlet baffles in the design. In this study, 18650 batteries reached a maximum of 38.9 °C at 0.5/1C. Moreover, the temperature difference was achieved at 7.3 °C (Jiaqiang et al. 2018).
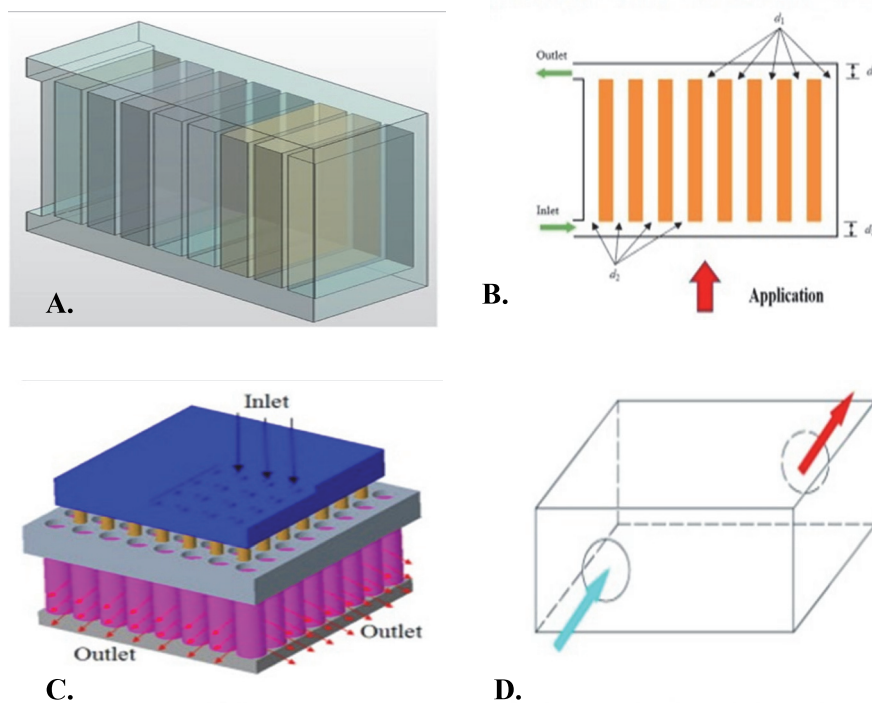
Figure 5. (A) Battery pack computing domain (Source: Peng et al. 2019). (B) Schematic diagram of the battery module (Source: W. Li et al. 2019) (C) Schematic of battery module using the air distribution pipe (Source: Zhou, Zhou, Xu, et al. 2019) (D) Lateral inlet and outlet (Source: Jiaqiang et al. 2018)

Yu et al. lowered the temperature of the lithium-ion battery pack by 8 °C by providing airflow. Yu and his colleagues conducted a numerical and experimental study using 180Ah prismatic lithium-ion battery cells. His team achieved a maximum temperature of 33.1 °C at 1C (Yu et al. 2014). Using dual silica, Li et al. managed a

numerical and an experimental study with prismatic lithium-ion battery cells. Li and his team achieved a maximum temperature of 47.4 °C at 5C (X. Li et al. 2019).
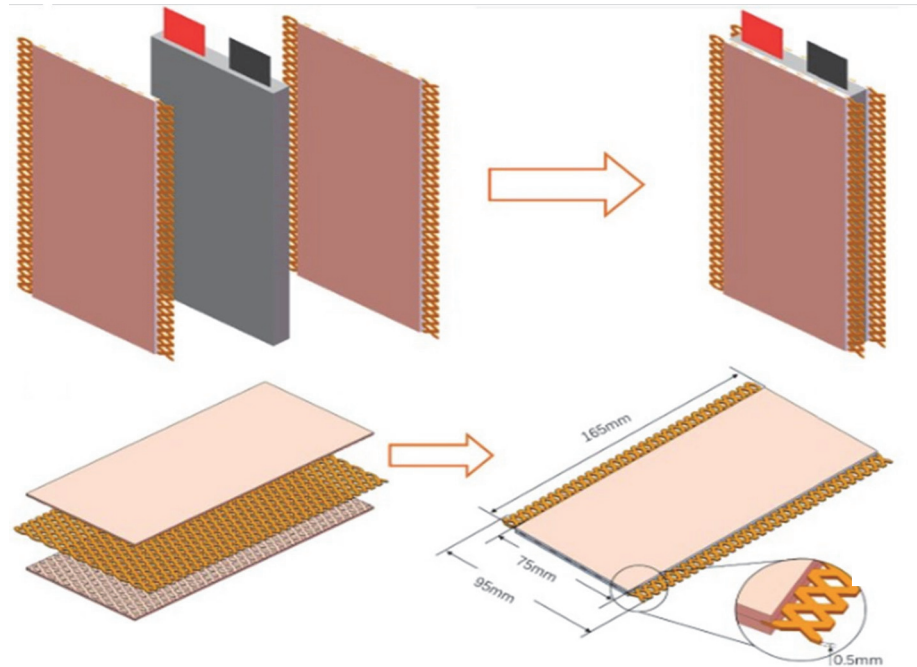
Figure 6. Cooling system and structure and geometry of the silica cooling plate with copper mesh (Source: X. Li et al. 2019).

2.2. Liquid Cooling

Lv et al. placed the graphene oxide-modified gel, which accelerated thermal conductivity, between cylinders. The lithium-ion pack was kept under thermal stability until 3C discharge, in this set up. Experiments were performed using 18650 cylindrical batteries. The cooling process carried out by water. The maximum temperature was 42 °C, and the temperature difference was 5 °C (Lv et al. 2019). Menale et al. tried to use different coolants in the battery pack. This approach gave numerous valuable data about the cooling capacities of variable coolants. These results indicated that cooling abilities of air cooling systems taking advantage of nothing but air shows severe limitations. Thus, the liquid flow should be used strictly. Menale and his team proposed a liquid-metal cooling system nearby water and silica gel coolers (Menale et al. 2019).

Gungor et al. worked with liquid cooling system based on canopy-to-canopy for thermal management. It has been documented that, the heat disparity in the battery cells is largely eliminated with a small mass flow rate, and battery temperatures are kept within the critical temperature values (Figure 8.) (Gungor, Cetkin, and Lorente 2022a).
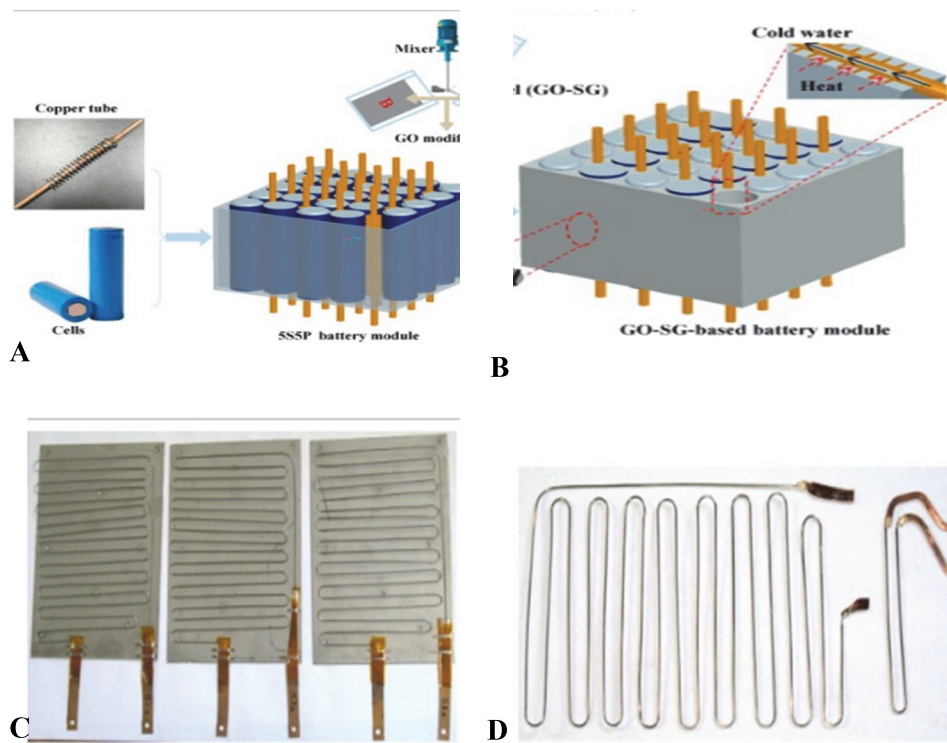
Figure 7. (A-B) Schematic diagram of the liquid cooling structure coupling the fins-enhanced cooling tubes with GO-SG (Source: Lv et al. 2019). (C) thermal resistances (D) a standard resistance and the additional one (Source: Menale et al. 2019).

Liu et al tried to cool batteries with a liquid obtained from the GA80IN20. They confirmed that it could be used for high c-rates. The numerical work was done using water and liquid metal, and the value was increased up to 5C. Overall, the maximum temperature was kept under 40 °C, and the temperature difference was measured below 5 °C (Liu et al. 2020). Zhou et al. argued that the contact zone and contact resistance are important parameters for liquid cooling. Therefore, Zhou and his team tried to use a jacket to place a battery inside in a liquid cooling method. In the numerical study, 18650 cylindrical batteries were used whereas water was preferred as the liquid fluid. The temperature of batteries reached to a maximum of 30.9 °C at 5C. The temperature

difference remained at 4.3 °C (Zhou, Zhou, Zhang, et al. 2019). Rao et al tried a new cooling system using variable contact surface. In the numerical study performed with a 26650 cylindrical battery, the battery was maintained below 40 °C at 3C (Rao et al. 2017). Shang et al. found that the inlet and a battery temperatures were inversely proportional to the heat sink using variable contact surfaces. A 20 Ah pouch cell was used in both numerical and experimental studies made with a mixture of water and glycol. Experiments were carried out in 1C and 2C, respectively (Shang et al. 2019).
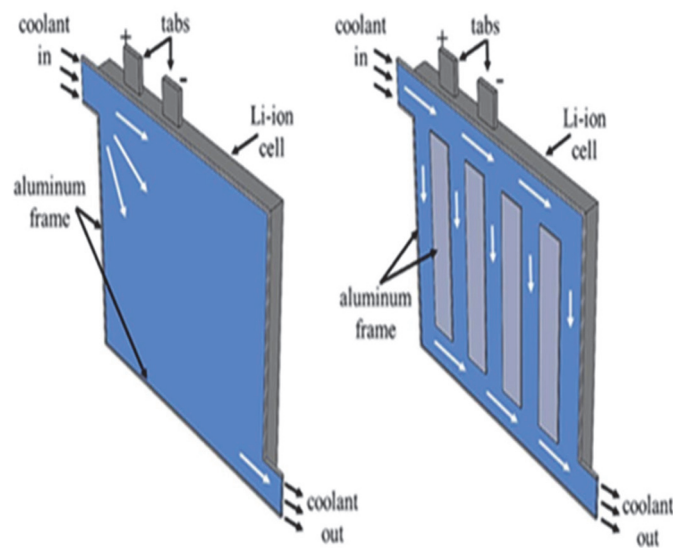
Figure 8. Cooling systems for reference case, canopy-to-canopy design
(Source: Gungor, Cetkin, and Lorente 2022a)
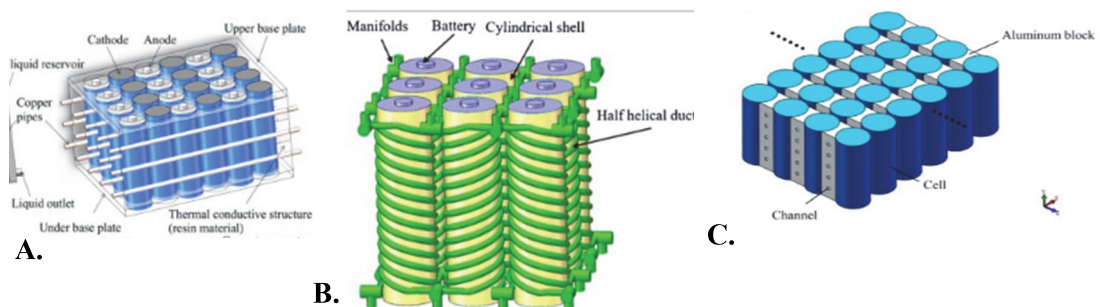
Figure 9. (A) Structure of battery pack and thermal resistance network from battery to copper pipe (Source: Liu et al. 2020). (B) Schematic diagram of battery module using half-helical duct (Source: Zhou, Zhang, et al. 2019). (C) Schematic of liquid cooling system for the battery module (Source: Rao et al. 2017)

Panchal et al. use zigzag type aluminum mini channels for creating cooling system. The experimental and numerical studies were analyzed and tested with 20 ah lithium-ion pouch cells. Water was used as the liquid fluid. The experiment was performed in 1C and 2C, respectively (Panchal et al. 2017). An et al. proposed a new channel for batteries. In this study, they conducted research using dielectric hydroflora liquid. They found that hydroflora liquid system could significantly reduce the maximum battery temperature. 20 Ah prismatic cell was used in the study, which was carried out at 1C, 3C, and 5C values. Additionally, NOVEC 7000 was used as a liquid cooler. Consequently, the maximum temperature was kept at 36.6 °C at 5C (An et al. 2017). Yates et al. used a cost-effective system composed of a heat sink and a cooling channel. In the numerical study, 18650 cylindrical batteries and coolant water were used. The temperature was kept below the maximum of 39.85 °C, and the temperature difference was kept at 3.15 °C at 5C (Yates, Akrami, and Javadi 2021).
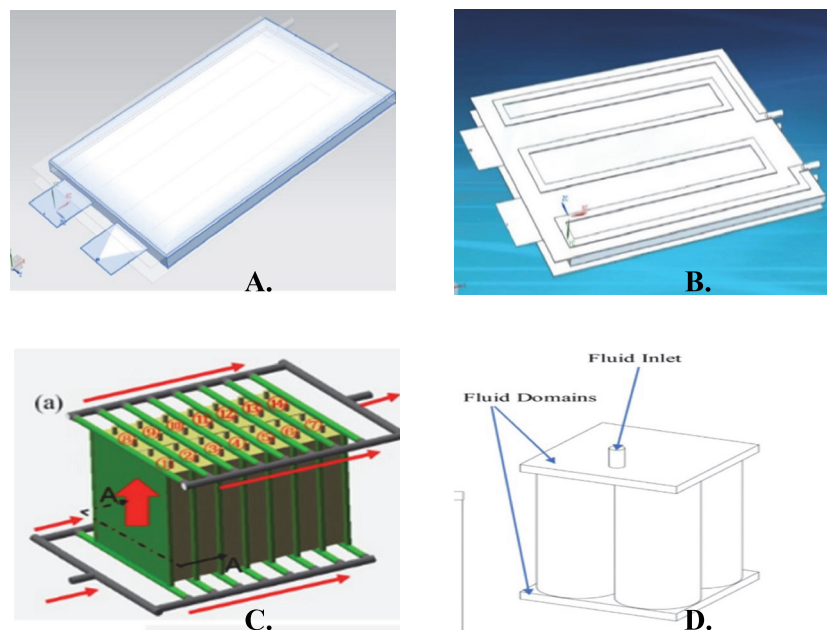
Figure 10. (A) Battery (B) Cold plate with battery (Source: Panchal et al. 2017) (C) Layout of battery module and coolant flow direction (Source: An et al. 2017) (D) Analysing the performance of liquid cooling designs in cylindrical lithium-ion batteries (Source: Yates, Akrami, and Javadi 2021)

Deng et al. developed a liquid cooling system using a sandwich method. Deng and his team evaluated effects of the liquid and the heat sink on the battery. In the numerical study performed with rectangular lithium-ion cells, the maximum temperature at 5C was

measured of 31.18 °C. Moreover, the temperature difference was identified at 1.15 °C (Deng et al. 2019). Du et al. discussed the cooling plate usage as a battery cooler. It was shown that input speed and packet width had a massive impact on battery charge time. Water was used as the refrigerant in both of their numerical and experimental study on 30 Ah pouch cells. According to results maximum of 32 °C was measured at 0.5C, 1C, and 2C. Furthermore, the temperature difference was found as 6.2 °C (Du et al. 2020). Xu et al proposed a new cooling system. The main idea was that the system with a T-shaped cooling structure might spread the flow to the entire battery pack. However, they reported that improvements are needed to disconnect the structure from the environment because the cold plate could not conduct the battery heat, efficiently. 70 Ah prismatic lithium cells were used in the numerical study. At 1C, the maximum temperature was 32.5 °C. When water was used, a 1.5 °C temperature difference was found (Xu et al. 2019). Li et al developed a cooling system using copper pipes. In this system, the heat generated by the batteries was planned to be transmitted to the copper pipes by the cooling plate. As a result, the temperature of the proposed system dropped below 41.92 °C with a liquid flow of 8 ml/s. Additionally, air cooling was added to the system for carrying out more efficient operations. Besides, in the numerical study performed with 3.65 volt 20 Ah prismatic lithium-ion, the maximum temperature at 5C was 41.92 °C. The temperature difference was found to be 1.78 °C (Y. Li, Zhou, and Wu 2019).
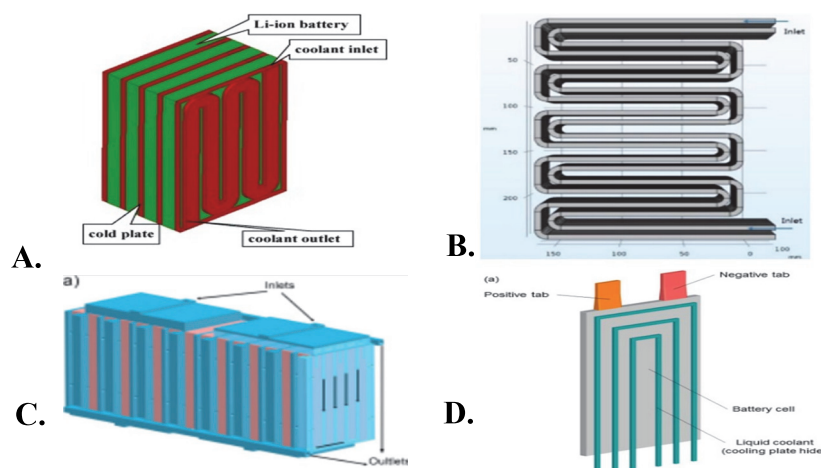
Figure 11. (A) The CFD model of battery pack.(Source: Deng et al. 2019) (B) The cooling channel structure(Source: Du et al. 2020) (C) Schematic of the water cooling system for 15 batteries (Source: Xu et al. 2019) (D) Geometry of single Li-ion battery cell with mini-channel cold plate (Source: Y. Li, Zhou, and Wu 2019)

Yang et al. used a combination of air cooling and liquid cooling systems. In detail, the maximum temperatures at 4C were 39 °C in experimental and numerical studies. The 4.4 °C temperature difference was measured when air and water were coolants to cool the 2 Ah 18650 lithium-ion battery (Yang et al. 2020). Huang et al. proposed a mini-channel cold plate design with the flow line concept resulting 44.52 % improvement in cooling performance. Rectangular lithium-ion batteries were used in the numerical study, and a water-ethylene glycol mixture was used as the coolant (Y. Huang et al. 2019). Chen et al. developed an optimization algorithm for the liquid cooling system. In this system, an 8 Ah lithium-ion cell was charged at 1C while water was used as a coolant. According to the results, the maximum temperature was achieved at 32.8 °C, and a 2°C temperature difference was found (S. Chen et al. 2019). Li et al. performed cooling by immersing the battery in a heat bath. The surface of the batteries was sealed with silicon. The system, which showed excellent cooling performance, had a rate of 3C and below 35 °C. 18650 lithium-ion batteries and water were used in the experiment carried out at 3C. Moreover, the temperature difference was 0.5 °C (X. Li et al. 2020).
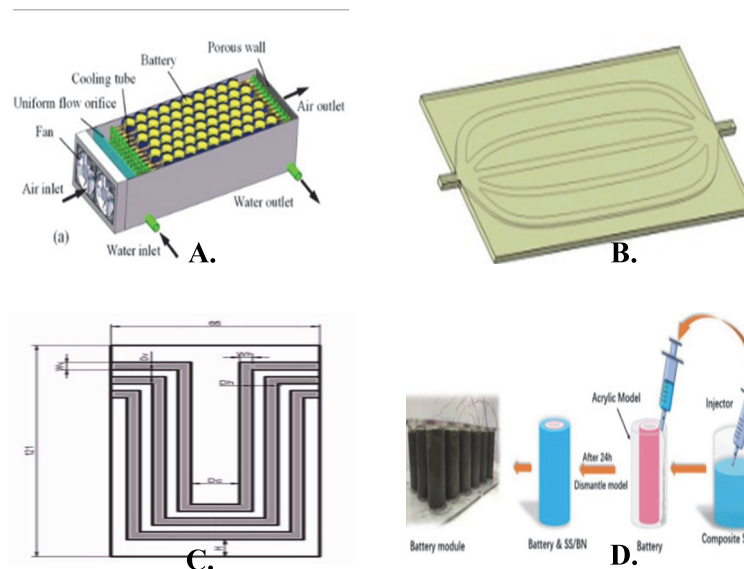
Figure 12. (A) Schematic diagram of the battery module (Source: Yang et al. 2020). (B) 3-Dimensional channels.(Source: Y. Huang et al. 2019) (C) The schematic diagram of the parameters of the cooling plate.(Source: S. Chen et al. 2019) (D) Battery coating process.(Source: X. Li et al. 2020)

2.3. Hybrid Cooling

BTMS can improve cooling performance by using multiple cooling methods instead of a single one. Tran et al. used heat pipes in the battery pack. It was indicated that the heat pipes reduced the thermal resistances of the batteries by 30 %. In the 7 Ah cylindrical lithium-iron study, the maximum temperature was 50 °C. (Tran et al. 2014). Further, Ye et al. developed the air/water heat pipe system and performed numerical and experimental calculations by using a 10 Ah prismatic lithium-ion cell. After the batteries were loaded at 8C, the maximum temperature reached 25-40 °C. Moreover, the temperature difference was 5 °C. It should be indicated that Ye emphasized that efficiency in cooling pipes is vital for heat pipe applications. (Y. Ye et al. 2015; 2016). Zhao et al. tested the efficiency of heat pipe with natural-forced convection and spray cooling. They proposed the water spray method. 3 Ah and 8 Ah were used to test system; the batteries were charged with 1C, 2C, and 3C, respectively. The maximum temperature was reported as 32 °C, and the temperature difference was measured as 2.5 °C (R. Zhao, Gu, and Liu 2015).
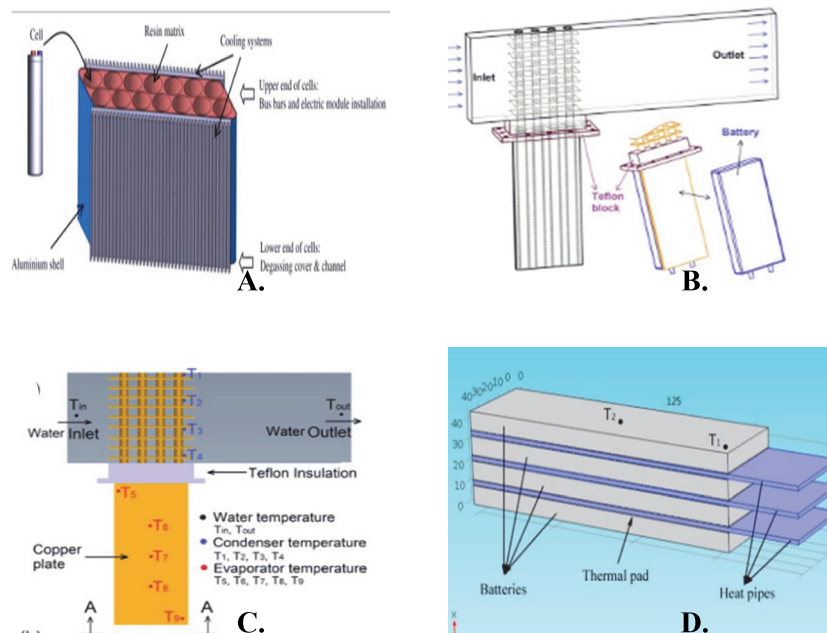
Figure 13. (A) Battery module.(Source: Tran et al. 2014) (B) heat pipe thermal management system(Source: Y. Ye et al. 2015) (C) Schematic of the experimental setup for characterizing the HPCP.(Source: Y. Ye et al. 2016) (D) Schematic illustrations of 8 Ah battery pack with heat pipes.(Source: R. Zhao, Gu, and Liu 2015)

On the other hand, Wang et al. immersed the ends of the heat pipes in a glycol/water liquid by using L-type heat pipes. The battery temperature was 41.1 °C under 4C discharge (Q. Wang et al. 2015). Ye et al. aimed to reduce the temperature difference by air convection using a micro heat pipe array (MHPA). Different designs with internal angles of 0, 5, 10, and 15 ° of micro-channels were used to obtain the most efficient angle supposed to be used, which was later identified as an angle of 5°. An 18 Ah prismatic battery reached a maximum of 40 °C with a 1C load.

Moreover, the temperature difference was detected at 5 °C (X. Ye, Zhao, and Quan 2018). Dan et al. conducted a numerical study with an air-cooled MHPA. They studied the cooling structures under different operating conditions and discharged the 55 Ah prismatic battery pack at 1C, 2C, and 3C. They found that the battery temperature was 40 °C. Besides, they detected a temperature difference of 2 °C between the batteries. (Dan et al. 2019). The use of PCM in the battery thermal management system can be associated with energy density because the high heat in the batteries can build up in the PCM and let the battery overheat. Therefore, it is inconvenient to use PCM alone. However, studies continue for a combined system. Ling et al. compared the cooling performance of PCM in air convection. First, they found that the battery maintains its temperature in just a few cycles with PCM alone. They suggested using the PCM in an air- and liquid-based combination. They used 18650 2.6 Ah lithium-ion battery cells. In the study, the batteries loaded with 0.5C - 1C reached 50 °C. (Ling et al. 2015)
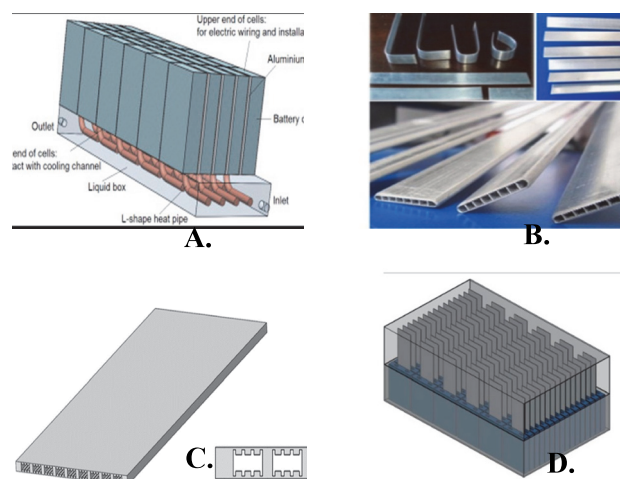
Figure 14. (A) Heat pipe BTMS demonstration.(Source: Q. Wang et al. 2015) (B) Schematic of MHPA.(Source: X. Ye, Zhao, and Quan 2018) (C – D) Schematic diagram of the MHPA thermal management system.(Source: Dan et al. 2019)

CHAPTER 3

MATERIALS and METHOD

3.1. Numerical Investigation

3.1.1. Discharge Characteristics

The heat generation of the batteries can be calculated by using the charge and discharge graphs of the batteries. A document containing the Molicel INR-21700-P42A cylindrical battery to be used in the battery pack and the graphics of this battery, ASPİLSAN Enerji Industry and Trade Inc. provided. This document has the battery's cell characteristics, physical properties, and charge and discharge curves.("INR-21700-P42A – Molicel" n.d.)

Nominal capacity specifies the quantity of charge, in ampere-hours (Ah), that the cell is rated to hold. As seen in Figure 15A, Molicel battery cells have a capacity of 4.2 Ah. Nominal voltage depends on the combination of active chemicals used in the battery cell. The rated voltage value is 3.6 V. The C rate measures cell electrical current. As Molicel battery cells are performance batteries, it can be seen in Figure 15A that they can rise to high C-rates. Since it can reach a discharge current of 45 amps, it has a discharge rate of about 10C. Cells are often first charged with either constant-current or constant-power. When the maximum permitted cell voltage is reached, the cell is held at that voltage until it is fully charged. It should be charged up to 4.2 V with a constant current of 4.2A, as seen in Figure 16A. Then, when the constant voltage and current reach 50mA, the charging process should be interrupted.

As seen in Figure 15B, the diameter and length dimensions of the battery are 21mm and 70mm, respectively. The battery can is steel. A short circuit is likely if the battery jacket is worn and deteriorated.

■ CELL CHARACTERISTICS

Capacity	Typical	4200 mAh 15.5 Wh
	Minimum	4000 mAh 14.7 Wh
Cell Voltage	Nominal	3.6 V
	Charge	4.2 V
	Discharge	2.5 V
Charge Current	Standard	4.2 A
Charge Time	Standard	1.5 hr
Discharge Current	Continuous	45 A
Typical Impedance	AC (1 KHz)	10 mΩ
	DC (10A/1s)	16 mΩ
Temperature	Charge	0°C to 60°C
	Discharge	-40°C to 60°C
Energy Density	Volumetric	615 Wh/l
	Gravimetric	230 Wh/kg

A.

■ PHYSICAL CHARACTERISTICS

Shape	Cylindrical
Can	Steel
Diameter	21.7 mm (Max)
Height	70.2 mm (Max)
Weight	70 g (Max)

B.

Figure 15. Molicel cylindrical battery cell (A) Cell characteristics (B) Physical characteristics. (Source: "INR-21700-P42A – Molicel" n.d.)

■ Charge Characteristics

A.

■ Discharge Rate Characteristics

B.
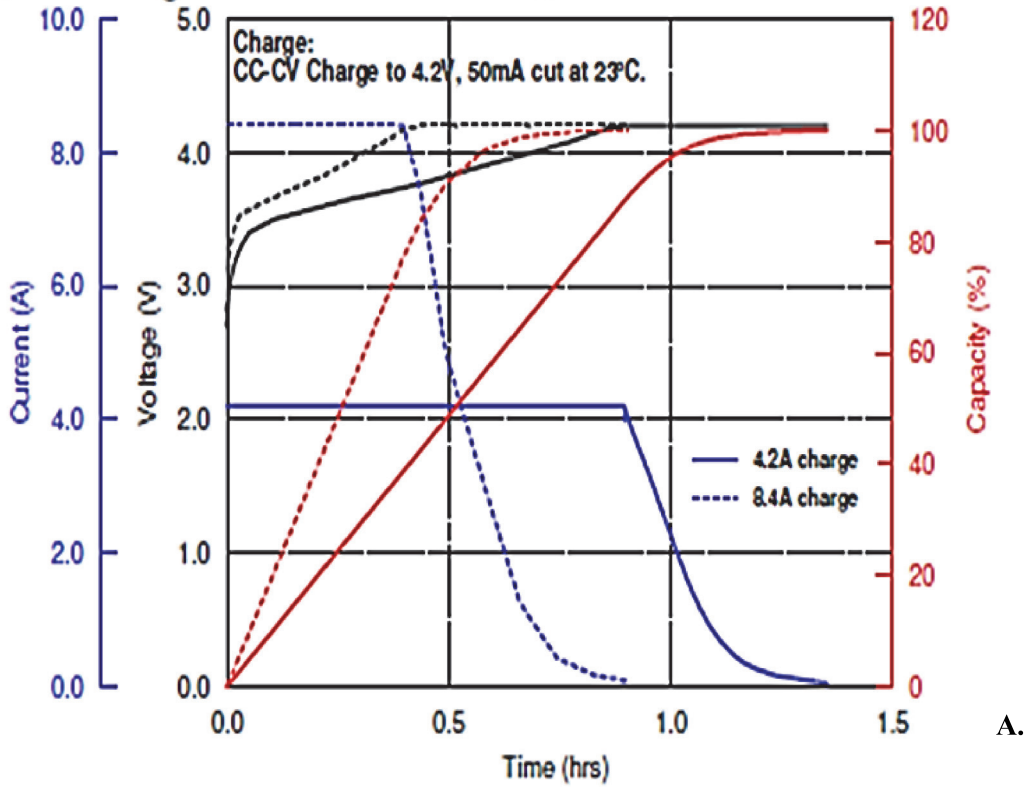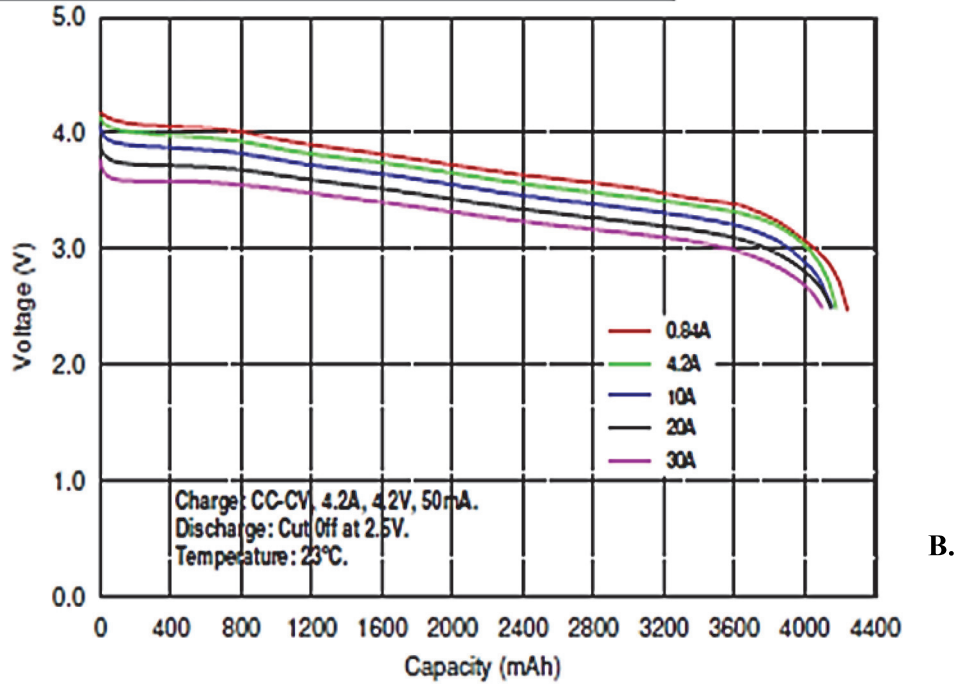
Figure 16. (A) Charge characteristics (B) Discharge rate characteristics
(Source: "INR-21700-P42A – Molicel" n.d.)

As shown in Figure 16B, voltage and capacity losses are observed when discharged at different amperage values at 23 °C ambient temperature. Because battery load is not in equilibrium, the measured voltage and battery capacity can change seriously from the equilibrium values and the further from equilibrium, the greater the deviation between battery voltage and capacity. This can be explained as the polarization effect. The voltage-capacity values at different C-rate seen in the Figure 16B must be to the desired format for the NTGK model in the ANSYS FLUENT program, which is used to determine the heat generation value of the battery. Values in the Voltage-Capacity graph (Figure 16B) were simulated in the MATLAB Simulink program at the values shown in the graph. The battery discharge model (Figure 17(A-B)) was created for each C-rate, including SoC-time, voltage-time, and current-time graphics.
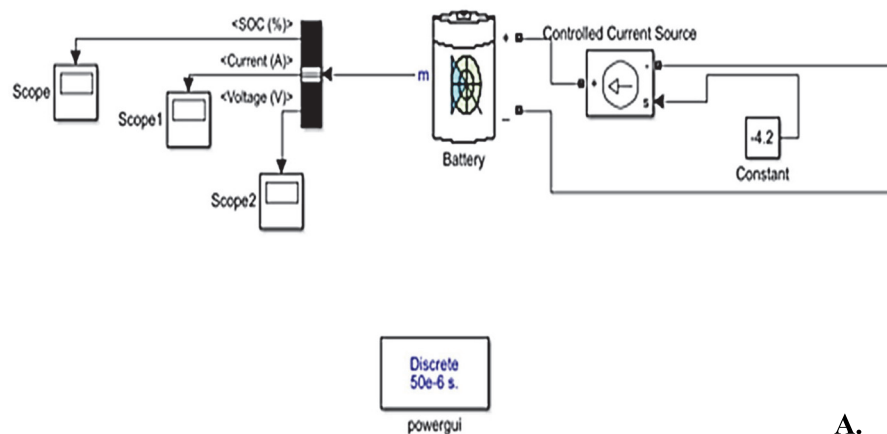
A.
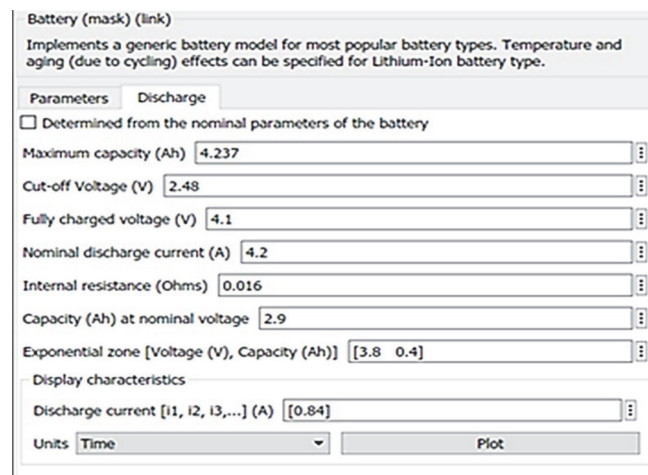
B.

Figure 17. Simulink battery model (A) Constant current discharge model (B) Battery parameters (Source: "Generic Battery Model - Simulink" n.d.)

A lithium-ion battery subjected to constant current discharge was built using Matlab Simulink. As shown in Figure 17(A), The power GUI component has been dragged into the model, and this component is required for any model that will use the custom power system library. The general battery component has been added to the model. Moreover, the general battery model parameters have been adjusted to customize the overall battery model. In this dialog box, under the parameters tab (Figure 17(B)), lithium-ion is selected, where you have the option to enable temperature and aging. Since aging and temperature data are not available, these effects will be unchecked. The rated voltage is set to 3.6 V and the rated capacity to 4.2Ah. Since the battery cells purchased from ASPİLSAN are original, the initial state of charge was left as 100. So at the start of the simulation, it was set to fully charged. Zero charge status will mean discharged entirely. The voltage discharge curves were adjusted at different current values as 0.84A, 4.2A, 10A, 20A, and 30A, respectively. Thus, discharge curves were plotted as a function of time.

The exponential zone is vital for the validation of the graph. This verification is required from Matlab, Battery tab. Volt and ampere-hour [3.8, 0.4] values in the region indicated by B in the Molicel battery discharge Graph were written to the Matlab. At the same time, the parameters seen in the graph were also used while creating the model. The fully charged voltage (A), exponential voltage-capacity point (B), nominal voltage (C), maximum capacity (D) required in Figure 16(B) are obtained from Figure 18. The lettering is shown here;

A = Fully charged voltage

B = Exponential voltage-capacity point.

C = Nominal voltage

D = Maximum capacity ("Generic Battery Model - Simulink" n.d.)

As shown in Figure 19, the yellow and gray areas have to do with the fitting process. The different discharge tab parameters change these areas; the yellow and the gray areas will change, and the shape of the discharge curves will change. If it is plotted against ampere-hour instead of the time, it is noticed that the extracted capacity is pretty similar at the five different discharge rates. The current control source seen in the system is connected to the battery. As shown in Figure 17(A), S port is a signal needed to tell the battery model how much current it is charging or discharging from the battery. As seen in the model Figure 17(A), a constant current block was used and connected to a constant current source. Negative 0,84 is entered to specify the current. So the current magnitude

is 0,84, and the sign indicates whether it is charged or discharged. Bus selector includes three different components in the Matlab model. By double-clicking the bus selector, the signals from the battery port can be seen, so the % charge status of the battery, current, and voltage information can be obtained from the port of the general battery. Finally, A constant current discharged lithium-ion battery model was created.
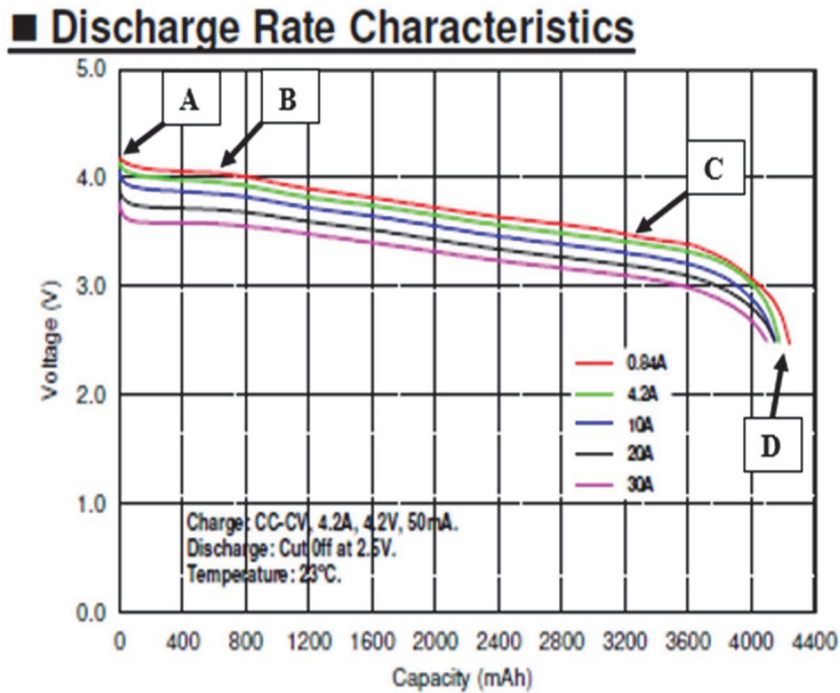
Figure 18. Parameterization and model validation
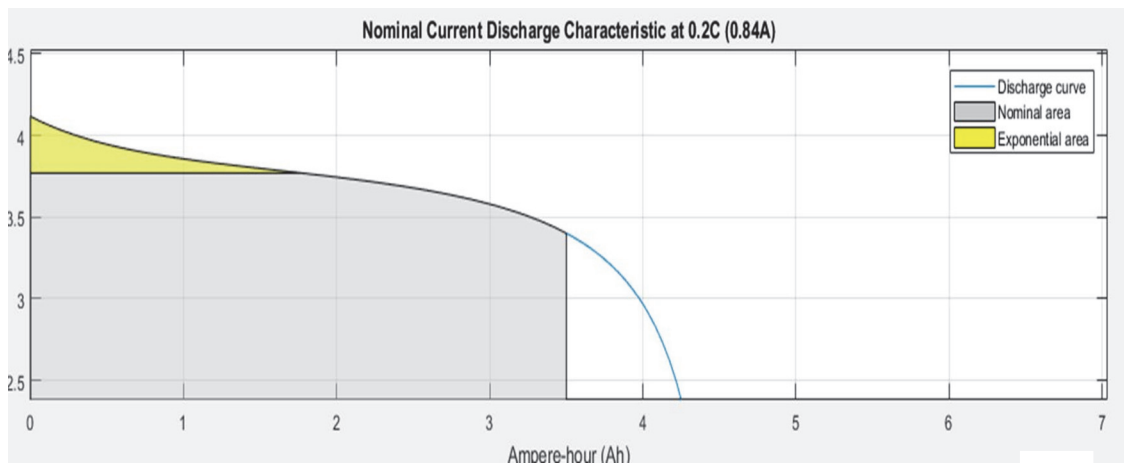
Figure 19. Discharge Characteristics

3.1.2. Battery Modeling

Air and water are considered as the coolant and the flow is calculate to be turbulance in all cases due to the low flow velocity but long characteristic lengths in this work. Furthermore, since the equations to be used in this direction are conservation of mass, momentum, and energy, they are expressed as follows:(Bejan 2013)

$$\frac{\partial \bar{u}_j}{\partial x_i} = 0 \qquad [1.1]$$

$$\frac{\partial}{\partial x_j}\left(\rho \bar{u}_i \bar{u}_j\right) = -\frac{\partial \bar{p}}{\partial x} + \frac{\partial}{\partial x_j}\left[\mu\left(\frac{\partial \bar{u}_i}{\partial x_j} + \frac{\partial \bar{u}_j}{\partial x_i}\right)\right] - \frac{\partial}{\partial x_j}(\rho \overline{u_i' u_j'}) \qquad [1.2]$$

$$\frac{\partial}{\partial x_j}\left(\rho \bar{u}_j \bar{T}\right) = \frac{\partial}{\partial x_j}\left(\frac{\mu}{\sigma_{cp}}\frac{\partial \bar{T}}{\partial x_j}\right) - \frac{\partial}{\partial x_j}(\rho \overline{u_j' T'}) \qquad [1.3]$$

Density, mean velocity, mean pressure, and dynamic viscosity are ρ, $\bar{u}$, $\bar{p}$, μ respectively. And K-epsilon model is used for viscous turbulent model and internal flows,

$$\frac{\partial}{\partial x_i}(\rho k \bar{u}_i) = \frac{\partial}{\partial x_i}\left[[\left(\mu + \frac{\mu_t}{\sigma_k}\right)\frac{\partial k}{\partial x_i}] + -\rho\overline{u_i' u_j'}\frac{\partial \bar{u}_j}{\partial x_i} - \rho\varepsilon\right] \qquad [1.4]$$

$$\frac{\partial}{\partial x_i}(\rho \varepsilon \bar{u}_i) = \frac{\partial}{\partial x_j}\left[[\left(\mu + \frac{\mu_t}{\sigma_\varepsilon}\right)\frac{\partial \varepsilon}{\partial x_j}] + C_1\frac{\varepsilon}{k}(-\rho\overline{u_i' u_j'}\frac{\partial \bar{u}_j}{\partial x_i}) - C_2\rho\frac{\varepsilon^2}{k}\right] \qquad [1.5]$$

$$\mu_t = \rho C_\mu \frac{k^2}{\varepsilon} \qquad [1.6]$$

Eddy viscosity, eddy dissipation rate, turbulence energy term, empirical coefficient, and turbulent Prandtl numbers are μ_t, ε, k, C_μ, σ_k, σ_ε, respectively.

The operating temperature range in batteries is essential. Battery life and safety depend on the operating temperature range. At Ansys, this is perfect for estimating the operating temperature range. The semi-experimental electrochemical battery model, the

NTGK module, is obtained with the multi-scale multi-domain approach to heat production of the cells. The heat generation of cells is time-dependent and inhomogeneous due to the thermal and electrochemical pattern. Newman, Tiedemann, Gu and Kim (NTGK) observed that the current density (A/m^2) varies linearly with cell voltage. The volumetric current transfer rate ("ANSYS Fluent Theory Guide" 2021):

$$j_{ECh} = \frac{Qnominal}{QrefVol} Y[U - (\varphi_+ - \varphi_-)] \qquad [1.7]$$

Qnominal describes the cell's total electric capacity, *Qref* is the experimental battery capacity. φ_+ *and* φ_- are phase potentials for + and - electrodes. U and Y are defined as a function of the battery depth of discharge (DOD). An experimentally measured polarization curve shows V, U at I=0. The inverse of the slope of the V-I curve shows the Y parameter. The set of equations recommended by the Ansys Fluent Theory Guide is as follows.("ANSYS Fluent Theory Guide" 2021)

$$U = (\sum_{n=0}^{5} a_n (DOD)^n) - C_1(T - T_{ref}) \qquad [1.8]$$

$$Y = (\sum_{n=0}^{5} b_n (DOD)^n) \exp\left[-C_2\left(\frac{1}{T} - \frac{1}{T_{ref}}\right)\right] \qquad [1.9]$$

a_n and b_n are experimental constants. C_1 and C_2 are electrochemical model constants. The electrochemical heat of reaction calculation is as follows:

$$\dot{q}_{ECh} = j_{ECh}[U - (\varphi_+ - \varphi_-) - T\frac{dU}{dT}] \qquad [1.10]$$

In the above equation, overpotential and entropic heat are seen. Conservation equations combined with thermal and electrical equations can be seen below.

$$\frac{\partial(\rho C_p T)}{\partial t} - \nabla(k\nabla T) = \sigma_+ |\nabla\varphi_+|^2 + \sigma_- |\nabla\varphi_-|^2 + \dot{q}_{ECh} \qquad [1.11]$$

∂ and T and represent thermal conductivity and temperature. σ_+ and σ_- are the effective electrical conductivities of the positive and negative electrodes.

Initial temperatures of 298K is used. The initial temperature of batteries is equal to air and water inlet temperature which implies that air and water at ambient temperature is utilized in BTMS. Velocity and pressure boundary conditions are used for the coolant at inlet and outlet boundaries, reactively. A no-slip boundary condition is used on all internal cooling channel walls.

A 3D model of a battery module, whose geometry and dimensions are given in Table 4, is developed. The battery cell, air, and liquid specifications are listed in Table 5. According to the parameters given in Table 4 and Table 5, the air and water flow are turbulent and the turbulence values are 8075 and 9029, respectively.

Table 4. 3D battery module, structural parameters

Parameters	Value[mm]
Length of the air inlet region	480
Height of air inlet region	70
Width of the air inlet region	58
Length of the liquid inlet region	480
Height of liquid inlet region	10
Width of the liquid inlet region	50

Table 5. Physical properties of the battery cell, air, and water
(Source: Gocmen and Cetkin 2022)

Parameters	Battery Cell	Air(298K)	Water(298K)
Density (kg/m^3)	2092	1.184	997.07
Specific heat capacity (j/(kg.K))	678	1007	4184
Thermal conductivity (W/(m.K))	18.2	0.02551	0.598
Dynamic viscosity (kg/(m.s))	---	1.15e-05	0.00089
Size(mm)	21x70	---	---
Velocity(m/s)	---	2	---
Mass flow (kg/s)	---	---	0.1

A.
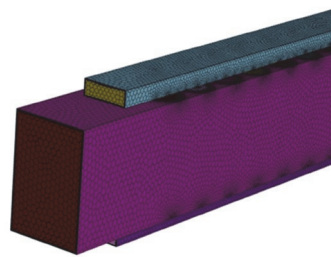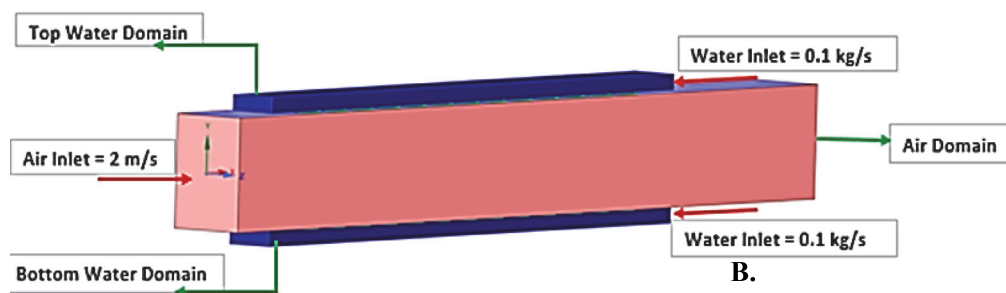
Top Water Domain
Water Inlet = 0.1 kg/s
Air Inlet = 2 m/s
Air Domain
Bottom Water Domain
Water Inlet = 0.1 kg/s
B.

Figure 20. (A) Battery meshing model (B) Developed battery module design

The polyhedral mesh was assigned using fluent mesh. The minimum orthogonal quality was found to be 0.3. As shown in Figure 20B, the pink area with 32 parallel-connected battery cells is the air channel. The blue zone is the water channel that acts opposite the air channel. In this model battery, heat, and fluid models were operated

together time-dependent. The simulations were solved with a time step of 0.1 s since the batteries operating at 10C would have a total discharge time of 6 minutes. For the air inlet velocity, it is 2 m/s. The water inlet velocity was determined as 0.1 m/s.
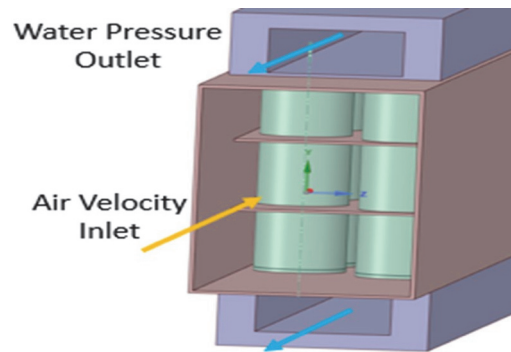
A.
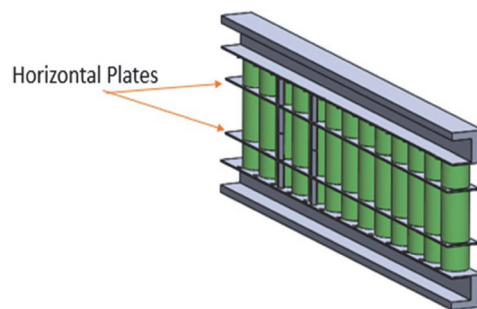
B.

Figure 21. Detail view of the developed battery module (A) Coolant directions (B) Heat plates

In the battery model shown in Figure 21A, the directions of the fluids are shown. Heat plates were placed between the battery to facilitate heat transfer. further, it was aimed to cool the tab of the battery with liquid and the body part with air.

3.1.3. Battery Casing and Components

Battery Pack consists of parallel-serial configuration, battery management system-controller, safety equipment, and connection organs (Table 6). All these elements

are in a metallic package that acts as a shock absorber, and they also have protective and stabilizing properties. (Figure 22)
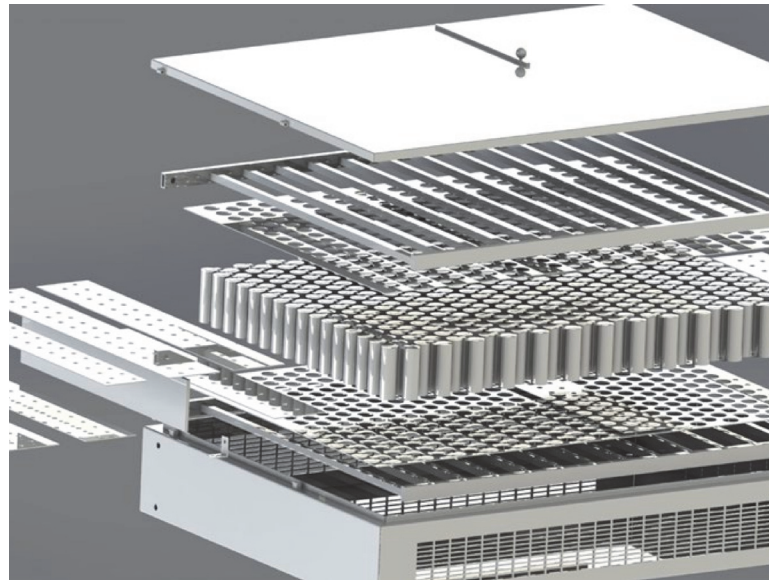
Figure 22. Battery pack explode view

Table 6. Battery pack components information

Piece	Component
1	Battery pack casing
2	Cooling channel
2	Cooling plate
384	Battery cell
768	Nickel strip
13	Busbar
768	M2 Nut and bolt

3.1.5.1. Busbar

The amperage of a busbar determines how much current it can safely carry. Wires have several standards that precisely specify what current can be carried safely, but not much has been written about busbars. Two related articles researched give knowledge about the current handling capabilities of industrial busbars. The Aluminum Association's first paper provides a DC table where rectangular busbars of various sizes are rated, and the second paper by Coneybear, Black, and Bush develops a model for deriving the amperages listed on the table. These articles can be used to determine suitable busbar sizes. Below are the equations used to calculate the capacity of a busbar, assuming a steady-state model:(Aluminum Electrical Conductor Handbook. 1989; Coneybeer, Black, and Bush 1994)

$$E_{in} - E_{out} + E_{gen} = E_{stored} \qquad \text{[1.12]}$$

$$E_{stored} = E_{in} = 0 \qquad \text{[1.13]}$$

$$E_{gen} = I^2 R \qquad \text{[1.14]}$$

$$E_{out} = hA_s(T - T_\infty) + \varepsilon\sigma(T^4 - T_\infty^4) \qquad \text{[1.15]}$$

$$I^2 R - hA_s(T - T_\infty) - \varepsilon\sigma(T^4 - T_\infty^4) = 0 \qquad \text{[1.16]}$$

$$I = \sqrt{\frac{hA_s(T - T_\infty) + \varepsilon\sigma(T^4 - T_\infty^4)}{R}} \qquad \text{[1.17]}$$

$$R = \rho_e L \frac{1 + \alpha_e(T - 20)}{A_x} \qquad \text{[1.18]}$$

Surface area, cross-section area, convection coefficient, resistance as a function of temperature, temperature, ambient temperature, emissivity, Stefan Boltzmann constant, electric resistivity at 20 ° C, and temperature coefficient of electric resistivity are A_s, A_x, h, R, T, T_∞ ε , σ, ρ_e, α_e Respectively.

This project considered the "minimum size scenario" for the busbar model since, in reality, the busbars will be in contact with the heat sink, which is optimized to cool the heat-generating batteries. Relevant sections can be selected from the busbars' nickel, aluminum, and copper table. When creating this table, the temperature rise was changed to the melting temperature of the selected material to optimize the sizing of the busbars fully. In the tables, the maximum current calculated with a safety factor of 1.5 was used as the desired current value. The graphs below (Figure 23) show the material selections and cross-sectional area options suitable for the busbars.
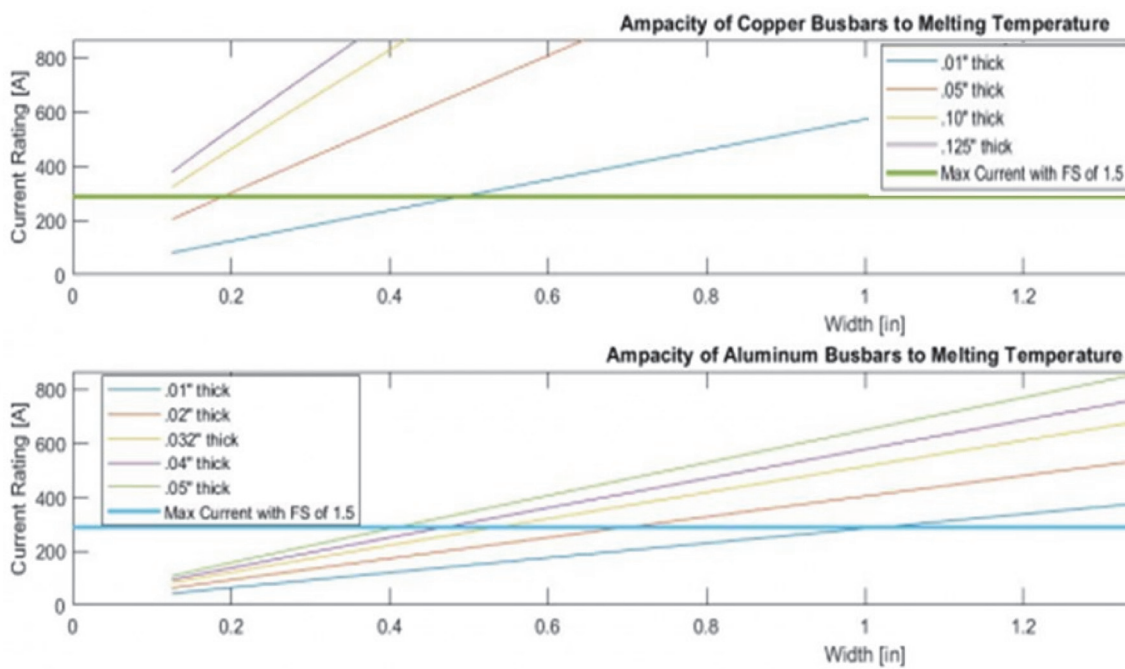
Figure 23. Minimum sizing for aluminum, and copper busbar

The choice of material for the busbars also largely depended on connecting the cells to the busbars. Choosing aluminum or copper limits the connection options, while nickel can be added using spot welding or laser welding. Ultimately, the decision comes down to price, and since material costs are high for nickel busbars and copper busbars, both bolted joining and spot welding can be used, so aluminum is the best material for this process.

Aluminum has been preferred for the plates that can carry a continuous discharge current of 134.4 amperes and a maximum discharge current of 268.8 amperes, considering its noticeably low mass density, easy workability, strength material price, and

thermal transmission properties. 80 mm width and 1.5 mm thickness (120 mm^2 cross-sectional area) carry the desired electrical load. Aluminum plate parameters in the analysis; (Table 7)

• Aluminum Sheet dimensions is 480x80x1.5 mm.

• Practical calculation for the cross-sectional area of the aluminum plate and the amperage on it:

$$Cross\text{-}sectional\ area\ X\ 0.9$$

• (Hole diameter) For 7 mm diameter:

$$16\ x\ 7 = 112\ mm$$

• Total cross-sectional area:

$$480 - 112 = 368\ mm\ ; 368\ x\ 1.5 = 552\ mm^2$$

$$A(min) = 368\ x\ 1.5\ x\ 0.9 = 496.8\ A$$

$$A(max) = 480\ x\ 1.5\ x\ 0.9 = 648\ A$$

• The melting point of aluminum is 660 °C.

• Aluminum plate is 150 grams. The total Aluminum plate weight is 2 kg.

• Film coefficient 25 W/mm^2 / °C L (Bobzin et al. 2019; Das et al. 2019)

• Density (kg/m^3) is 2700.

• Thermal conductivity (W/m.K) of aluminum is 250.

• Electrical conductivity of aluminum is 36 mS/m.

• Electrical resistivity of aluminum 28 Ω.m x 10^{-8} at 20 °C

Aluminum is lightweight, durable, malleable and corrosion-resistant. This metal is widely used for components in the aerospace, transportation and construction industries.

• Non-corrosive

• Easily machined and cast

• Lightweight yet durable

• Non-magnetic and non-sparking (Bobzin et al. 2019; Das et al. 2019)

Table 7. Physical properties of the metals (Source: "AWG - American Wire Gauge Converting Chart" n.d.; "American Wire Gauge Chart and AWG Electrical Current Load Limits Table with Ampacities, Wire Sizes, Skin Depth Frequencies and Wire Breaking Strength" n.d.; "Understanding the Neher-McGrath Calculation and the Ampacity of Conductors" n.d.; Das et al. 2019)

Properties	Copper	Nickel	Aluminum
Thermal conductivity (W/m.K)	390	99	205
Density (kg/m³)	8900	8500	2700
Electrical conductivity (mS/m)	59	12.9	36
Melting point (°C)	1083	1455	660
Electrical resistivity (Ω.m x 10^8)	17	78	28

The analysis steps made on the model created in Ansys Mechanical with these parameters are summarized in Figure 24:
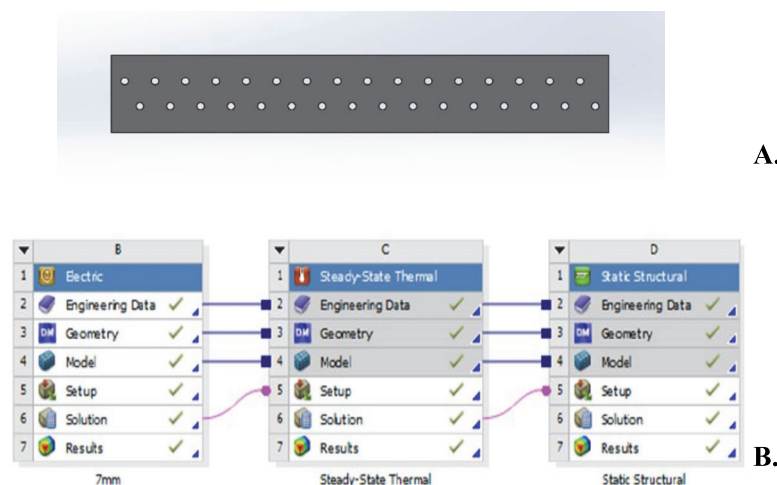
Figure 24. (A) Busbar design (B) Analysis process

First of all, the theoretically calculated electrical properties were verified with the analysis program, and the temperature and deformation results were evaluated.

3.1.5.2. Battery Casing
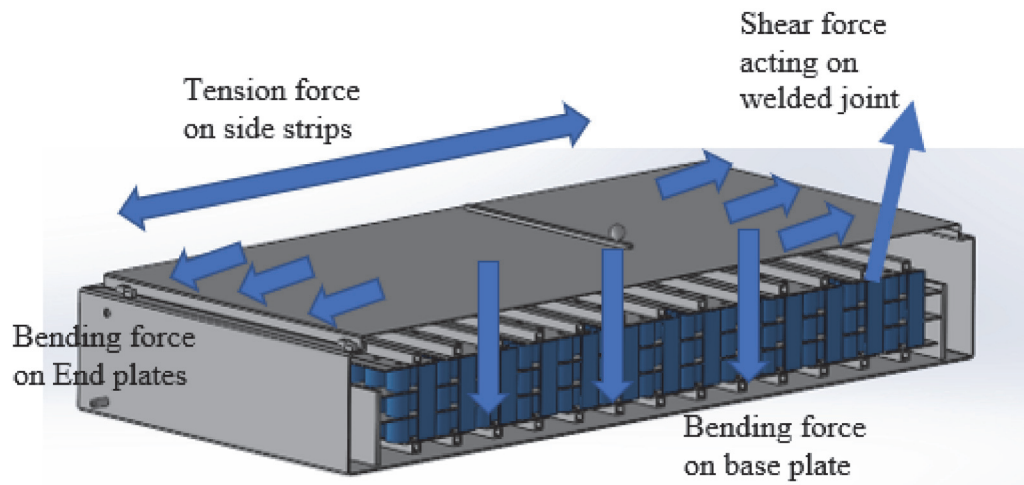
Figure 25. Forces acting on the battery pack

The first force acting on the battery pack is the tension force on the side strips. They create pressure due to a lateral tension on the cell surface. The cell surface constrains the endplate. With the action of the side strips and the endplate, the cells will show a bending force. All weight acts on the base plate. The dominant force on the base is the bending force. And there is spot welding on nickel strips and busbars. There is a shear force on these materials. The dominant forces on the side strips, end plates, base plate, nickel strip and busbars are tension force, bending force, bending force, and shear force, respectively.(Ashby n.d.)

Stress is the internal resistance offered by the body to the external load applied to it per unit cross-section area. σ, F, A_0 represent stress (Pa), force(N), cross-section area(m^2), respectively.(Ashby n.d.)

$$\sigma = \frac{F}{A_0} \hspace{3cm} [1.19]$$

Strain is the deformation of material that result from an applied stress. ϵ, L, L_0 represent strain, length after load is applied (mm), original length (mm), respectively.

$$\varepsilon = \frac{L - L_0}{L_0} \qquad\qquad [1.20]$$

The design of the base plate is very important. The task of the base plate is to protect the cell load from bending, cracking and degradation. If bending starts, cell constraint changes. If cell constraint changes, the busbar cannot be constraint. If the busbar cannot be constraint, the battery pack will fail. If the design is rectangular, the width and length of the plate can be estimated. Because the battery sizes are known. But the thickness must be calculated.(Ashby n.d.)

This analysis is under the condition that;

- Continuous rectangular plate, constant thickness
- Uniformly distributed weight of battery pack

$$\text{Total area} = \text{Length x width (mm}^2) \qquad\qquad [1.21]$$

$$Q = \text{Total force / Total area (N/mm}^2) \qquad\qquad [1.22]$$

After the load is calculated, the Ashby methodology can be followed to select the material. Ashby methodology consists of 4 parts. In the translation section, the objective function should be determined. In the translation section, objectives such as minimum cost, minimum weight or maximum power can be determined for the base plate. The second part is screening. In this section, maximization or minimization is done. It is necessary to maximize power so that the thickness of the base plate is reduced. Or, if the cost is to be reduced, the density of the material should be minimized. The third section is the Rank section. In this section, it is necessary to list the properties between the two materials. The maximize function must be written. A bending force is on the base plate. By using this homogeneous force, it is desired to reduce the thickness and increase the strength.(Young, Budynas, and Sadegh 2012)

$$\text{Maximize } \frac{E^{\frac{1}{3}}}{\rho C_M} \qquad\qquad [1.23]$$

E, C_M, ρ represent modulus of elasticity, cost of material, density of the material, respectively.

$$t = \sqrt[3]{\frac{-\alpha q b^4}{E\gamma}} \qquad\qquad [1.24]$$

t, E, γ, b represents thickness, modulus of young, maximum deflection, breadth.(Young, Budynas, and Sadegh 2012)

Mechanical phenomena play an essential role in battery module operation and safety requirements. During operation, battery modules are subject to dynamic loading and random vibrations that can cause short circuits and fire. Strength values such as torsion, buckling, shearing, and bending were taken into account when choosing the material of the battery pack casing. Suppose materials with different thermal expansion are combined, and heat is generated at the contact interface. In that case, the inhomogeneous thermal expansion can cause shear load and, in severe cases, plastic deformation or breakage in the contact area, adversely affecting the contact behavior and, therefore also, joint resistance.(Zwicker et al. 2020)

Table 8. Comparison of international standards for drop test of HV/EV batteries (Source: Safe Drop Test Measurements for HV Electric Vehicle Batteries | CSM GmbH n.d.)

Region	International	USA	Korea	China
Standard	SAE J2464	UL2580	KMVSS 18-3	QC/T743
Drop Height (m)	2	1	4.9	1.5
Surface	Flat Surface	Concrete	Concrete	Wood

Materials in the literature;

Metal: Aluminum, steel

Plastic: ABS, PC

Composite: CFRP, Aramid-Kevlar

A low thermal expansion value, high thermal conductivity, high specific heat capacity (Cp), and thermal dissipation values were considered among the materials. In addition to these, economic, availability, and density values were compared. DKP material has been chosen because the battery pack casing is more durable and lighter in the results obtained by performing drop and impact analyses of many materials. DKP sheet material is less costly than other battery pack casing materials.

DKP material has been chosen because the battery pack casing is more durable and lighter in the results obtained by performing drop and impact analyses of many materials. DKP sheet material is less costly than other battery pack casing materials. The 780x580x160 mm DKP sheet casing package is calculated with the battery dimensions and other material dimensions to be placed inside
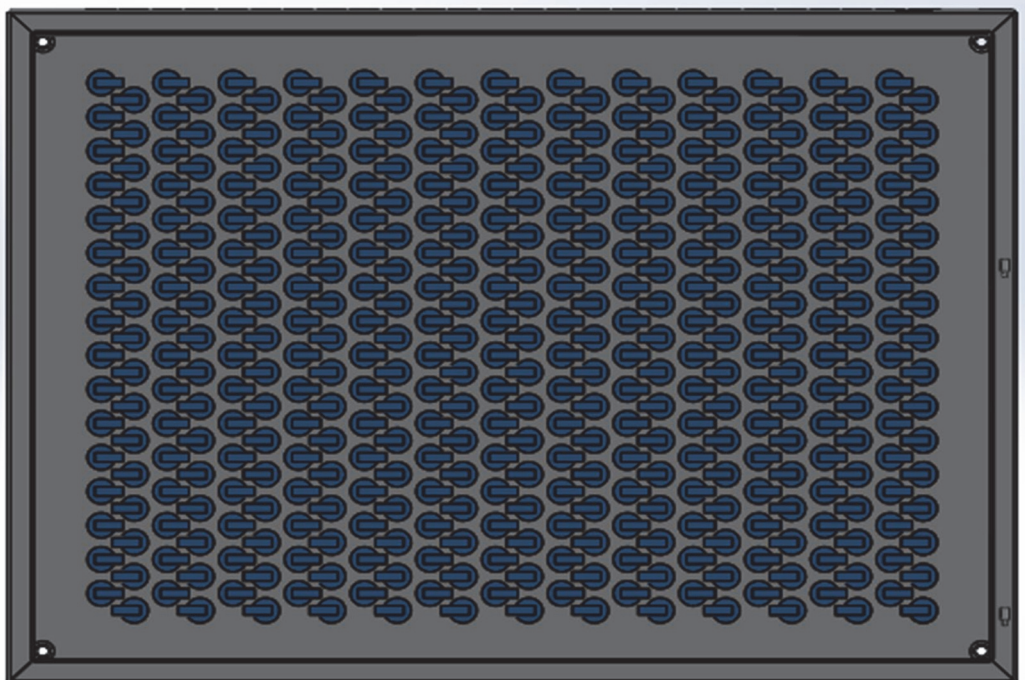
Figure 26. Battery cell and battery casing design

Table 9. Casing material properties
(Source: The Formability of Erdemir 6112 Sheet Metal by the Hydromechanical)

Material	Mechanical Properties	
DKP Sheet metal 6112	Tensile strength, Mpa	350
	Yield strength, Mpa	252.9
	Elastic modules, Gpa	141.7
	Poission's ratio	0.28
	Specific weight, g/cm^3	7.83

Drop test studies evaluate the impact of a part or assembly with a rigid or flexible planar surface. The program automatically calculates the impact and gravity loads. No other loads or restrictions are allowed. Allows the following options to set up the drop test: It can be define the drop height (h), the gravitational acceleration (g), and the direction of the impact plane. The program calculates the velocity (v) at impact as follows: $v = (2gh)^{1/2}$. The body moves in the direction of gravity as a rigid body until it hits the hard plane. The program solves a dynamic problem as a function of time. General equations of motion:

$$F_I(t) + F_D(t) + F_E(t) = R(t) \qquad [1.25]$$

Where $F_I(t)$ are inertial forces, $F_D(t)$ are damping forces, and $F_E(t)$ are elastic forces. All of these forces are time-dependent. In static analysis, this equation boils down to $F_E(t) = R(t)$ because inertia and damping forces are neglected due to small velocities and accelerations. External forces include R(t), gravitational, and impact forces.

The software uses an explicit time integration method to solve drop test runs. It automatically estimates the critical time step based on the smallest element size and uses a smaller value to avoid bias. Very small elements can suppress when appropriate or use

mesh checking to prevent the creation of very small elements. The program internally adjusts the time step as the solution progresses.("Drop Test Studies - 2020 - SOLIDWORKS Help" n.d.; Jacob, Goulding, and National Agency for Finite Element Methods & Standards (Great Britain) 2002)

Table 10. Drop analysis setup information

Type	Drop height
Drop Height from Centroid	2000 mm
Gravity	9.81 m/s^2
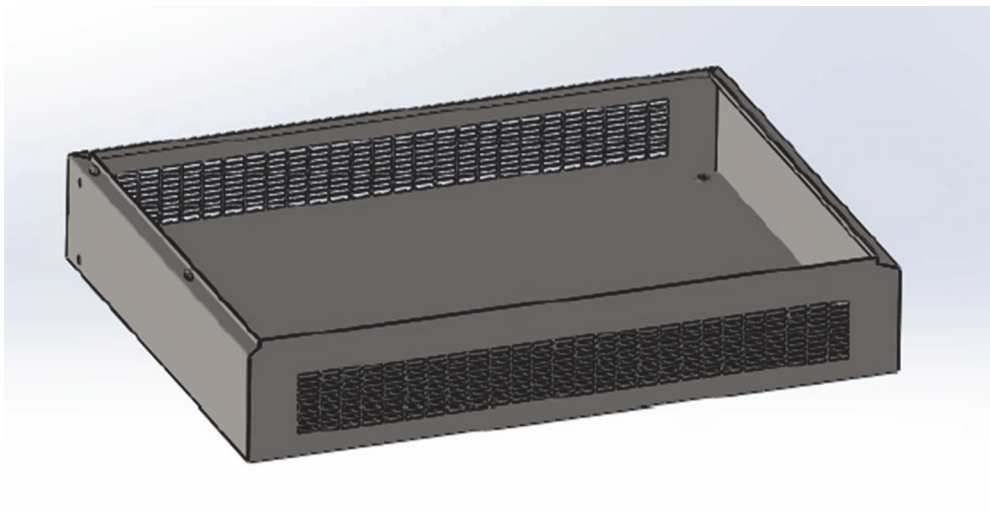
Figure 27. Battery casing design

The battery casing package has cooling channel inlet and outlet holes, ventilation channels, and positive-negative terminal channels. Analysis was carried out by homogeneously adding 35 kg battery weight into the 2 mm DKP metal model.

CHAPTER 4

EXPERIMENTAL METHOD

4.1. Structural Setup

Battery pack drop tests are planned in 2 phases. Firstly, free fall from 2 meters will be applied for the base part. Secondly, the drop procedure will be applied for the edge of the package from 2 meters.

The dimensions of the battery casing are 580x780x115 mm. 8 stones were placed in the package prepared for the drop test homogeneously. Stone wool was placed on the top and bottom parts of the package. The size of the stones is 198x163x80 mm. And a stone is 4.5 kg. The total weight of the stones is 36 kg. There is 2 kg base sheet in the package. The weight of the package is 20 kg. The package is approximately 60 kg. As shown in Figure 28, the steel wire was cut and dropped after the battery pack was tied with a steel wire from its four sides and lifted to 2 meters with a crane.

Figure 28. Drop test for base plate

Figure 29. Drop test for edge

A 60 kg battery pack dropped from 2 meters was dropped in 0.63 seconds. And the falling speed is 6.24 m/s.

4.2. Thermal Setup

Figure 30. Battery pack charge setup with 15A

The figure shows that the experimental setup was prepared using a liquid circulator, charger, thermocouple, and fan. The charger is 48V 20A. The circulator provides a 23-degree water flow. Furthermore, it will be used to cool the tabs of the batteries. The fan will dissipate the heat on the surface of the batteries.
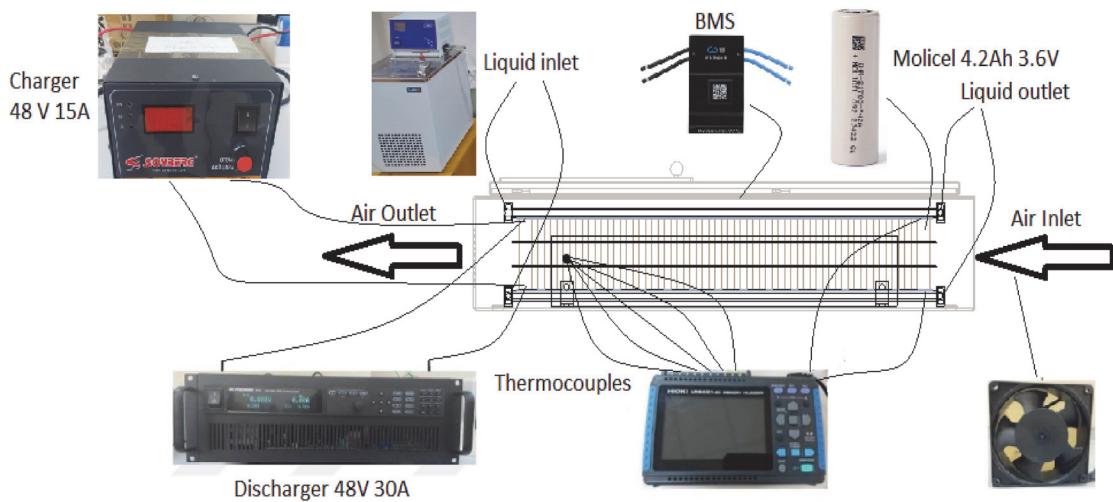
Figure 31. Scheme of charge and discharge setup

You can see the schematic of the experimental setup in the figure. Air inlet and outlet, fluid inlet and outlet are visible.5 Thermocouples are placed in the warmest place in the flow channel. The diagram shows that charging and discharging were done at different amperes. The discharge process is 48V 30A. BMS will save battery cells in many adverse conditions. It protects overcharge, over-discharge, overtemperature, under temperature, overvoltage, and BMS temperature. With the Bluetooth link, it is possible to see all axioms in the battery pack. Data can be saved with the CANbus connection. At the same time, the BMS shows the charge rate of the battery pack. The error rate is low since the cloump counter is used in the SoC. BMS provides a very good balance between battery cells. It distributes the current to all cell groups with its 2A distribution capacity.

The cells used in the battery pack are 4.2A and nominal 3.6V. Battery cells have a high discharge feature. Since the battery cells can be discharged up to 10 C, are called high performance batteries. As seen in the figure, battery temperatures do not give thermal runaway up to a maximum of 60 degrees.

Capacity	Typical	4200 mAh
		15.5 Wh
	Minimum	4000 mAh
		14.7 Wh
Cell Voltage	Nominal	3.6 V
	Charge	4.2 V
	Discharge	2.5 V
Charge Current	Standard	4.2 A
Charge Time	Standard	1.5 hr
Discharge Current	Continuous	45 A
Temperature	Charge	0°C to 60°C
	Discharge	-40°C to 60°C
Energy Density	Volumetric	615 Wh/l
	Gravimetric	230 Wh/kg

Figure 32. Battery cell specification

CHAPTER 5

RESULTS and DISCUSSION

5.1. Numerical Result

5.1.1. Discharge Characteristics

Table 11. Voltage-time values in seconds and volts

0.84 A MATLAB		4.2 A MATLAB		10 A MATLAB		20 A MATLAB		30 A MATLAB	
TIME(s)	V	TIME(s)	V	TIME(s)	V	TIME(s)	V	TIME(s)	V
3.35	4.13	2.02	4.09	0.94	3.96	0.49	3.80	2.59	3.70
21.47	4.11	8.78	4.08	4.91	3.94	2.55	3.79	3.67	3.69
78.08	4.10	19.60	4.06	10.03	3.93	5.21	3.78	4.74	3.68
⋮	⋮	⋮	⋮	⋮	⋮	⋮	⋮	⋮	⋮
17060.27	2.79	3490.92	2.79	1446.63	2.79	717.15	2.77	452.20	2.78
17087.44	2.78	3496.33	2.78	1450.04	2.78	718.62	2.75	453.46	2.76
17121.40	2.76	3501.74	2.76	1453.45	2.76	720.10	2.74	454.71	2.75
17155.37	2.74	3507.14	2.75	1456.86	2.74	721.28	2.73	455.97	2.74
17182.54	2.73	3512.55	2.73	1459.70	2.72	722.46	2.71	457.04	2.73
17209.71	2.71	3517.96	2.71	1461.97	2.71	723.64	2.70	458.12	2.71
17236.88	2.70	3522.02	2.70					458.83	2.71

Some of the voltage-time values of the discharge process with five different values are shown in the Table 11. When the battery is discharged with 0.84A, 4.2A, 10A, 20A, 30A, the discharge times are 17236.88s, 3522.02s, 1461.97s, 723.64s, 458.83s respectively. As seen from the Table 11, the simulation was interrupted at 2.7 V., And batteries were not allowed to die. All results of voltage-time values are available in the chart below.
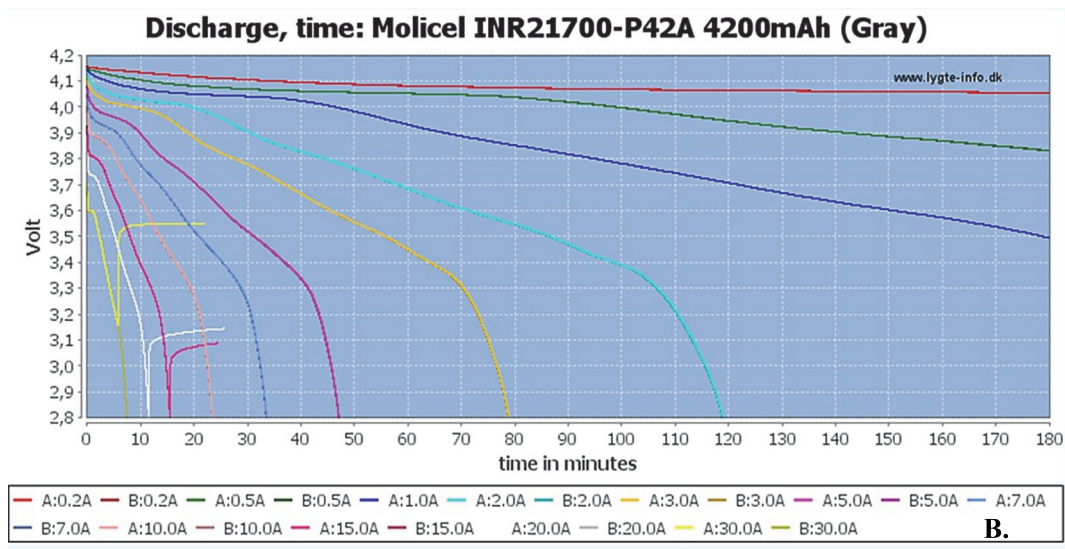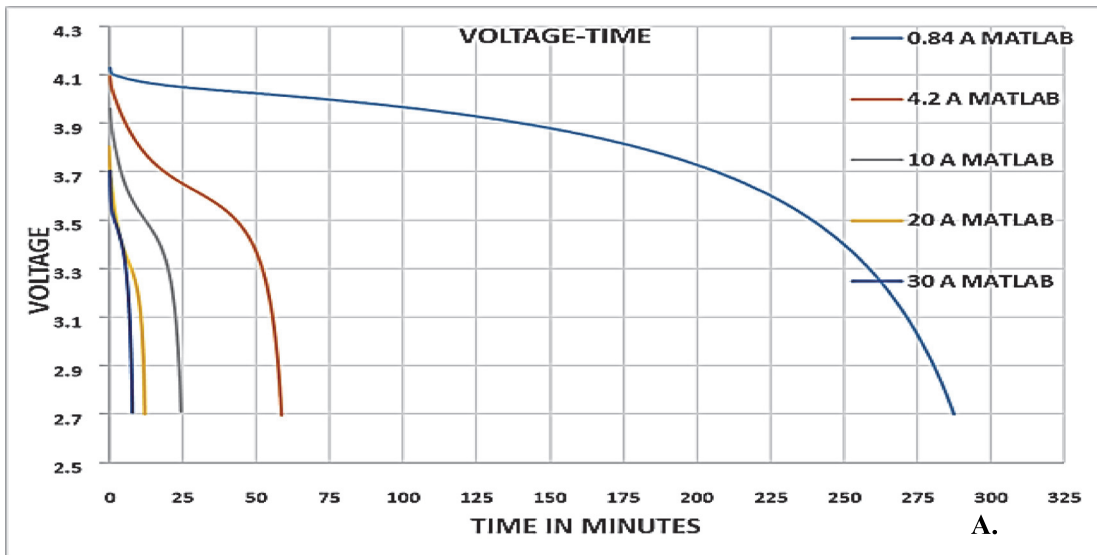
Figure 33. (A) Voltage-time graph obtained from Matlab (B) Experimentally obtained
voltage-time graph (Source: "Test of Molicel INR21700-P42A 4200mAh
(Gray)" n.d.)

The experimental discharge study for 10A, 20A, and 30A for Molicel and the
results obtained from Matlab above are similar. In Figure 33(A), 0.84A, 4.2A, 10A, 20A,
30A are represented by the colors blue, red, gray, yellow and dark blue, respectively. In
Figure 33(B), 10A, 20A, 30A are represented by the colors pink, purple, white, and
yellow, respectively. After the voltage data is obtained, it must be loaded in Ansys Fluent
. NTGK Model is selected as seen in the Ansys. Then, the temperature and voltage data
from which we obtain the battery voltage data are added to the system. Thanks to Ansys
parameter estimation, battery features have been added to the system.

5.1.2. Battery Modelling

When the molicel battery cell is discharged at 10C at Ansys Fluent, the voltage/SoC-time graph is obtained.

Cell Voltage/SoC vs Time
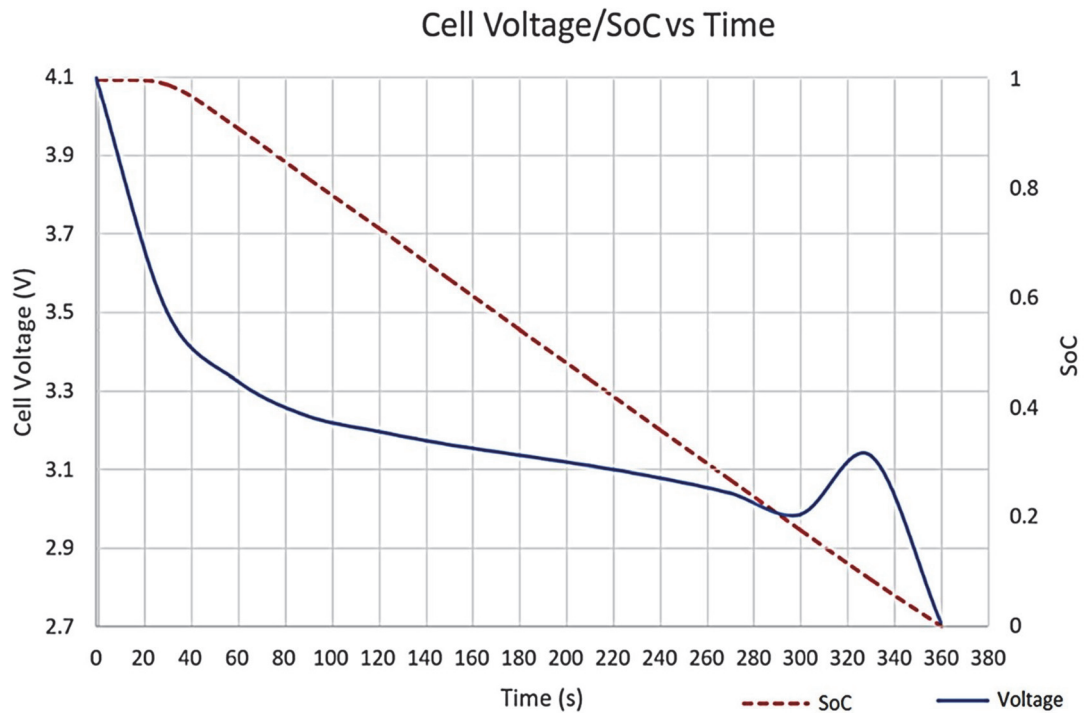
Figure 34. Time-dependent variation of voltage and SoC values as a result of simulation

As seen in Figure 34, voltage and SoC are coloured blue and red, respectively. The SoC drops from 1 to 0 while the voltage drops from 4.1 to 2.7. And the analysis takes 360 seconds.

In the discharge simulation at 10C without using cooling, the temperature value increased up to 411 Kelvin. Although the maximum temperature at which the battery will rise is 333 Kelvin, the value resulting from the simulation may cause a thermal runaway of the battery.

The temperature values obtained in the discharge process at 1C and 10C are shown above. The batteries need to stay between 298K-308K values to prevent changes in capacity values. Even looking at these values, it becomes clear that cooling is required during charging and discharging.
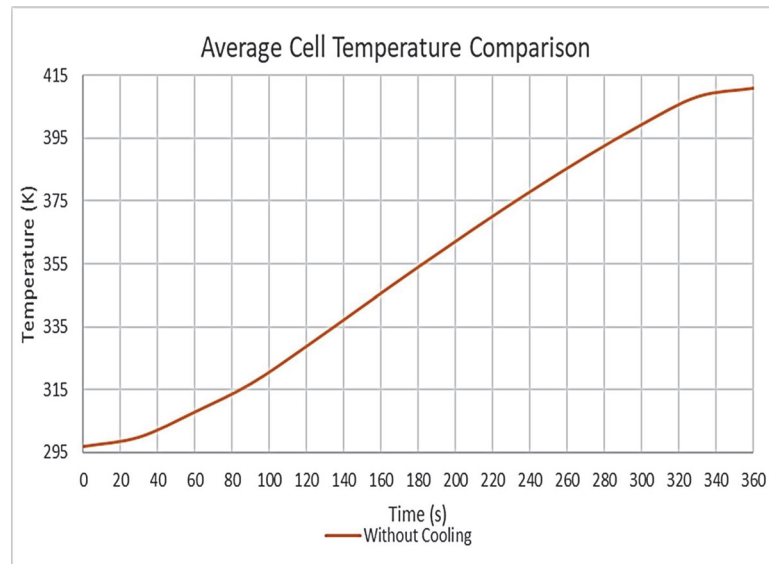
Figure 35. The average temperature change in the cells depending on the time during discharge at 10C
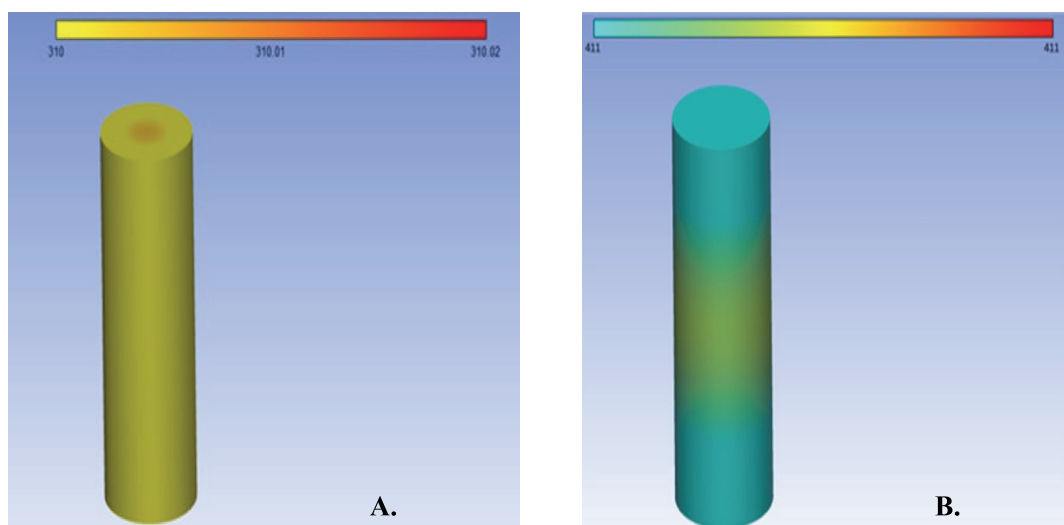
Figure 36. Discharge of battery cells at (A) 1C and (B) 10C

5.1.3. Spacing Between Battery Cells

After temperature mapping of one cell, optimum spacing studies were performed for the cell group. A 2D model was created by between 1-10 mm gaps. The maximum heat flux obtained at 1C is defined for the region of the battery cells. Air inlets and outlets are shown in Figure 37. As can be seen in Figure 37, the gap dimensions are defined with

S. Symmetry boundary conditions are used when the battery module and the expected pattern of the flow/thermal solution, have mirror symmetry. As seen in Figure 37, the symmetry boundary condition is defined to the battery module.
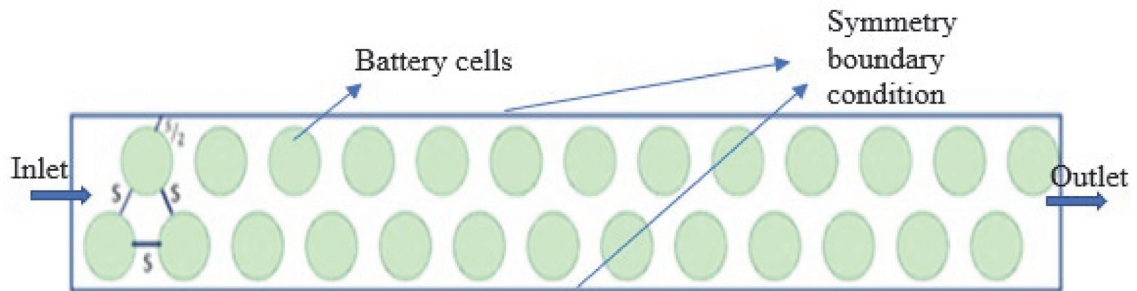
Figure 37. 2D battery module mesh model
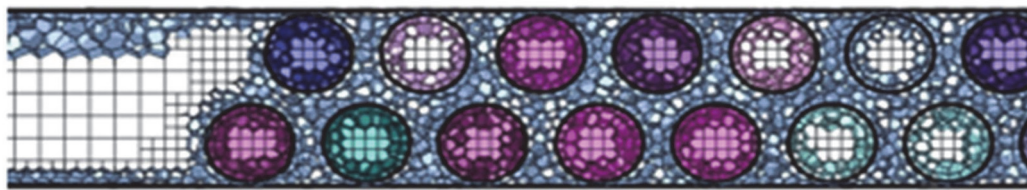
Figure 38. 2D battery module spacing model

The polyhedral mesh was assigned using fluent mesh. The minimum orthogonal quality was found to be 0.1 in Figure 37. In this study, different simulations were made, starting with the distance between them 1 mm and up to 10 mm. The distance between the battery cells also determined the overall size of the battery pack.

The literature believes that the distance between cells can be estimated for battery packs of specific capacity. The optimum gap between the battery cells was investigated during the 1C discharge in the study. The primary inputs are this model's 2 m/s air velocity and 298 K air temperature. Since the model is a 2D study, heat flux is defined instead of battery's heat generation. Heat flux was obtained from the battery simulation in 1C. This value is 90 W/m^2.

To see the effect on temperature distribution of the gap size on the battery model, the conservation of mass and momentum equations between 1 and 20 mm in Figure 39 were solved. According to Figure 39, the battery module average temperature from 1 to 8 mm gap show an effective decrease. The temperature difference in 8 mm gap is

15.188K. The battery temperature difference from 8 mm to 20 mm is 0.432K. These results show that the dimension of gap in the battery cell partially affects the temperature after a specific value.
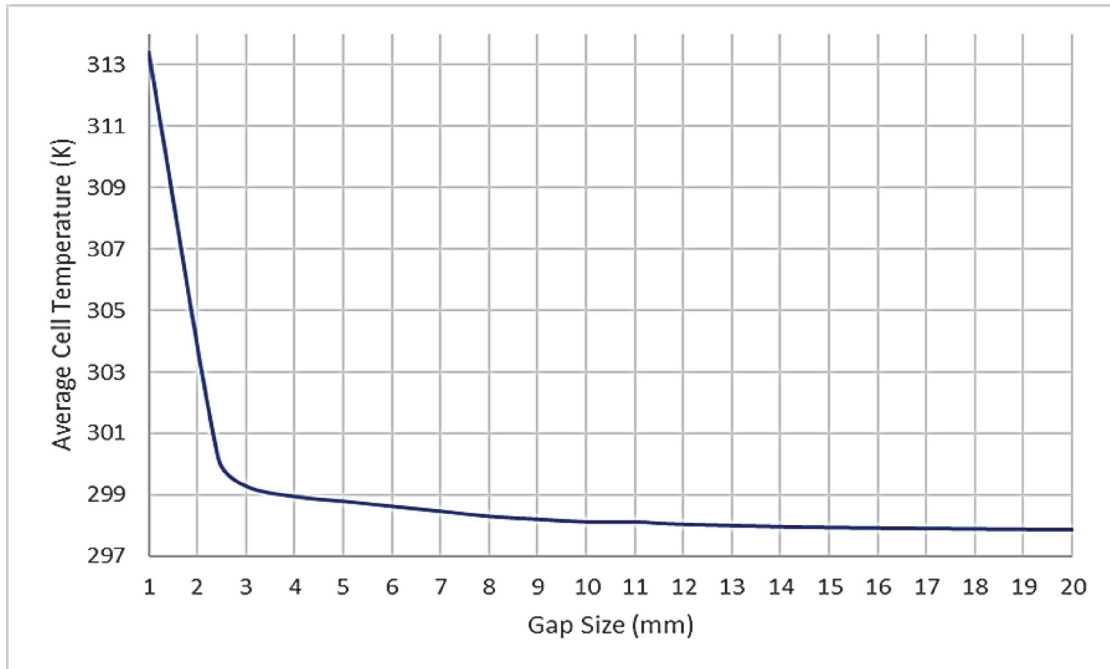
Figure 39. Temperature-gap relationship as a result of parametric simulation
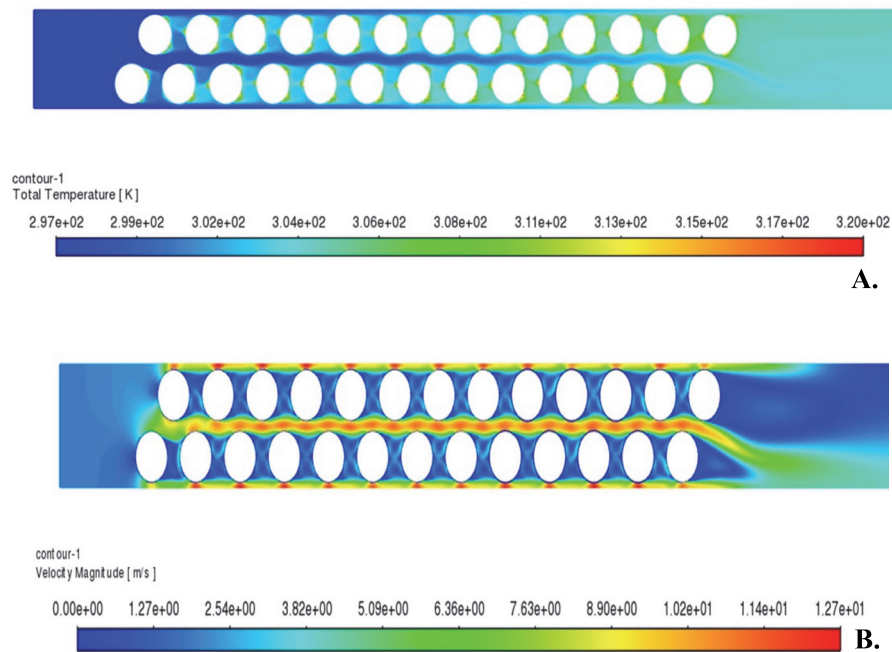
Figure 40. As a result of the simulation-based on 90 W/m^2, (A) temperature and (B) velocity values

The max temperature decreased from 400K to 320K by 8 mm space between the cells. As a result, the battery cell placed with a gap of 8 mm were obtained between the desired temperature. As can be seen in Figure 40(B), the velocity magnitute has reached 12.7 m/s. As the velocity magnitude increases, the noise in the battery module increases. Therefore, it is aimed not to exceed 15 m/s speed throughout the analysis.

5.1.4. Simulation of Battery Module

As seen in Figure 41, when the battery module is discharged at 10C using air and water cooling, the heat transfer coefficients are 0.11, 0.46, and 0.47 W/ (m^2 K), respectively. Air, bottom water domain, and top water domain are represented by green, yellow, and blue.
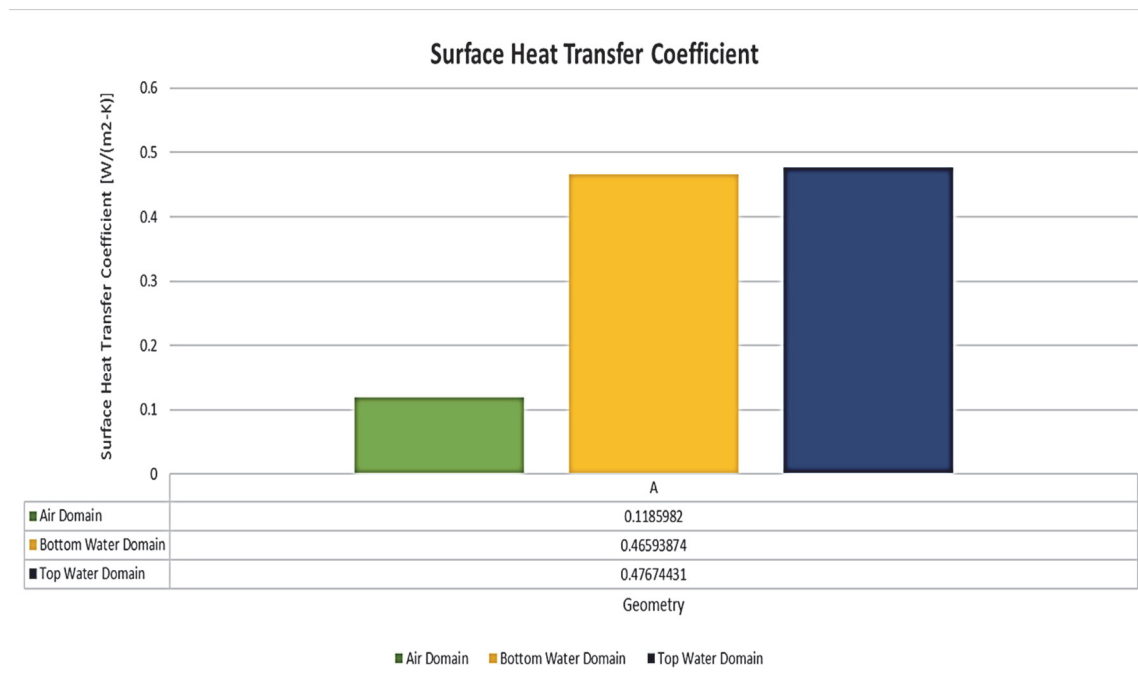
Figure 41. Surface heat transfer coefficient

As can be seen in Figure 42, the maximum temperature reached 313K when battery air and water cooling is used.
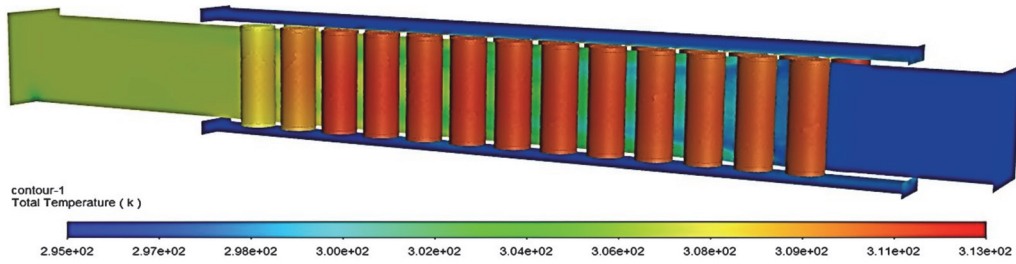
Figure 42. The cell temperature contour for cooling with all domain
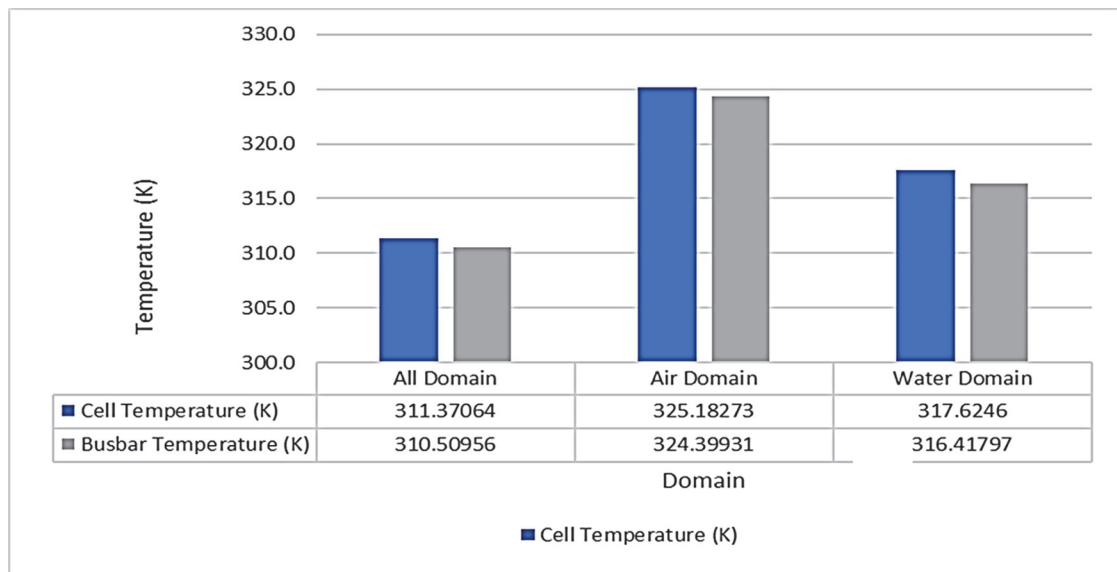
Figure 43. Water and air temperature comparison on the cells and busbar ; only using air domain, only using water domain, and using all domains

As seen in Figure 43, cell temperatures and busbar temperatures are represented in blue and gray, respectively. This Figure 43 is arranged to examine the all cooling domain, the air cooling domain and the water cooling domain separately. The cell temperatures reached 325.18K only in the air cooling domain, while the busbars reached 324.39K. When only the water domain was examined, the cell temperatures were found to be 317.62K, while the busbar temperatures were found to be 316.41K. When the all domain was examined, the cell temperatures were found to be 311.37K, while the busbar temperatures were found to be 310.50K.

5.1.5. Battery Casing
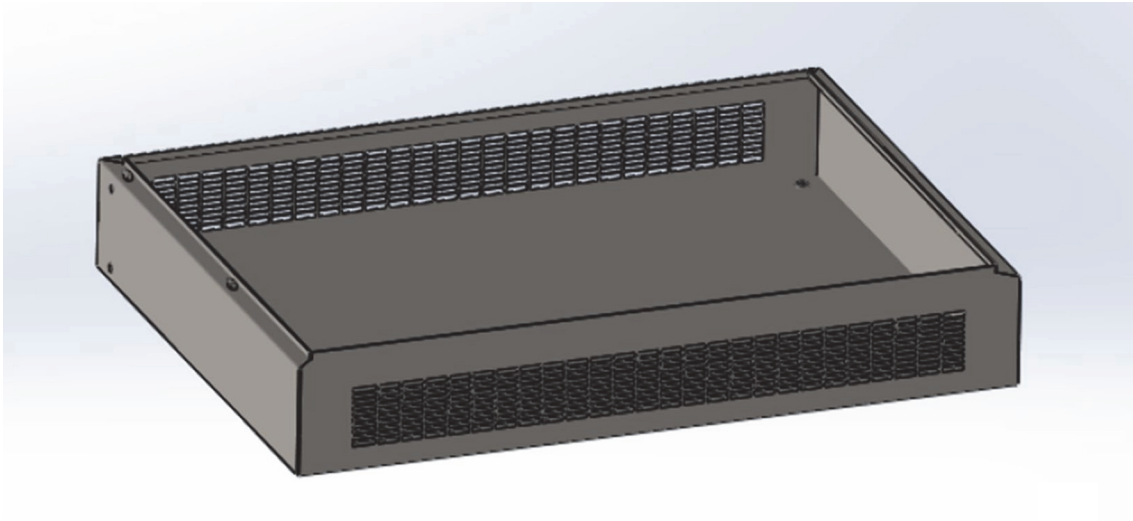
Figure 44. 3D battery casing model

The drop test study is a specific type of dynamic analysis used to model the impact force of a short time duration event. The dynamic problem means forces and displacements are changing with time. This impact could be on a component or assembly with a rigid or flexible plan or surface for the impact. It should be an explicit direct time integration method to solve the problem. The battery pack has two components, a battery casing and a battery cell. It will drop from a height of 2 meters on a planar surface. Plasticity is important for accurate results. The permanent failure can be seen through plasticity von mises. And assembly model is fully bonded. Solidworks suggest solution time based on geometric calculation. This solution time is based on model geometry, material properties, and elastic wave propagation.

$$t = 3L/\mu \qquad \text{[1.26]}$$

$$\mu = \sqrt{\frac{E}{\rho}} \qquad \text{[1.27]}$$

Where time, geometry, elastic wave propagation, elasticity module, density are t, L, μ, E, ρ, respectively. It is related to time, geometry and elastic wave propagation. Elastic wave propagation is related to modulus of elasticity and density.("Drop Test Studies - 2020 - SOLIDWORKS Help" n.d.)

According to the SAE conditions in the literature, the battery casing recommends that it be dropped from 2 meters to a flat surface. Therefore, in the Solidworks simulation, the package's displacement and yield stress results, for which 2 meters drop analysis was performed, were monitored. The gravitational force on the 2 mm sheet metal and the 35 kg battery module force inside the model were defined.
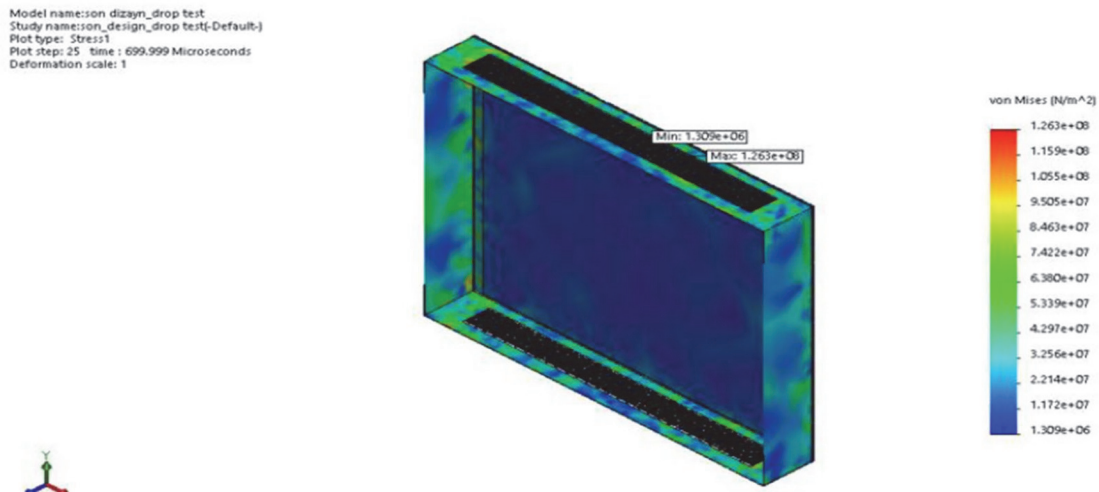
Figure 45. Stress contour of battery casing when drop test at gravitational force

According to the results, within 0.5 seconds after the battery casing drops, the maximum yield stress in the battery casing is $1.263\text{x}\,10^8$. The yield stress of the sheet metal, which was also mentioned in the material method section, is $2.529\text{x}\,10^8$. Therefore, the battery casing is in the safe zone.

54

5.2. Experimental Result

5.2.1. Mechanical Result

Since the aluminum plates are not available soldered or spot welded, the connection between the nickel and the battery is provided with M2 bolts. The short circuit is prevented by placing M2 bolts in the middle of the busbar and avoiding contact with the batteries. An M2 hole was drilled with a drill to connect the nickel strips with bolts. Then the k values of M2 bolts are 1.20 mm. After 832 M2 holes were drilled on the aluminum plates, the top parts of the drilled holes were enlarged due to countersunk bolts. It is notion that this process is essential not to affect the cooling channel on the aluminum plate. Further the 16mm bolts are shortened after the nuts are installed to eliminate the possibility of a short circuit.

There are 32 parallel and 1 serial battery pack on the aluminum heat plate. A total of 64 batteries are connected to an aluminum plate (64 nickels, 64 bolts, 64 nuts). There are 32 parallel batteries in the positive and negative terminals. 832 M2 bolts-nuts and 832 22x8x0.2 mm nickels were used on the heat plate. The plates, which play an essential role in creating the battery pack, have cooling and stabilizing features. It helps to maintain the rigidity of the battery by contacting the battery at two points. The plates are aluminum, more suitable material in terms of thermal and physical properties. The heat plates are 700x490x1.5 in size, and the hole diameters on them are 21.7 mm. After the plates were modeled, they were made ready for assembly by laser cutting. Then aluminum was welded with 5 mm thick side supports. For the cooling pipe to be easily placed in the battery pack, the inlet and outlet discharge pipes have been threaded, and they have been provided with the feature of plugging and unplugging.

Two packages were produced. One pack is for battery assembly, and one pack is for drop tests. The cover of the package made for battery assembly is made of plexiglass to see the inside easily. When the cover of the package is closed, it is locked with a double-point locking system. By placing 3 hinges between the cover and the body, complete contact of the o-ring with the body is ensured.

BMS dimensions are 102x162x17.95 mm. Furthermore, its weight is 400 grams. 80 m of space is reserved in the package. Moreover, cable joints are covered with insulation material.
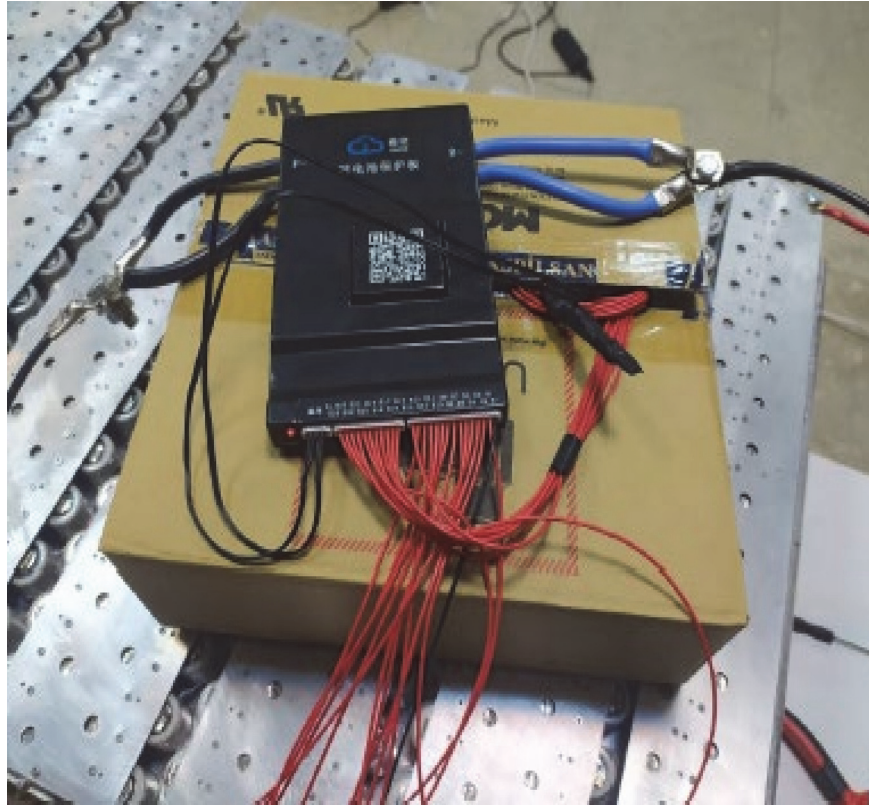
Figure 46. BMS connections

As seen in Figure 46, the battery pack is controlled by BMS. BMS actively performs cell current balancing. A maximum of 2A current is sent to the batteries. The cables shown in red in Figure 46 are connected with positive busbars. The black and blue wires on the BMS are the negative terminal wires. BMS is activated with 5V.

A cooling channel was placed inside the battery pack. The inlet and discharge pipes are combined with a leak-proof gasket. Then, silicone was sprayed into the holes in the package to prevent any external leakage.

Silicone was used to fix the battery cells. Then busbars welded cells. SUNKKO 709 AD+ was used in this spot welding process. Sunkko 709 AD+ spot welding is specially designed for lithium-ion. It can spot welding nickel strips between 0.05 and 0.3 mm for nickel-plated steel and between 0.05 and 0.25 mm for pure nickel strips.

Busbars and nickels shown in Figure 47 are connected with bolts. A spot welding machine is suitable for pure nickel, nickel-plated steel, nickel-plated iron, iron and other alloys. A spot welder cannot weld metals such as copper and aluminum. Then, nickel strips were spot welded to the battery cells.

Figure 47. Welding nickel strips to battery cell with Spot welding
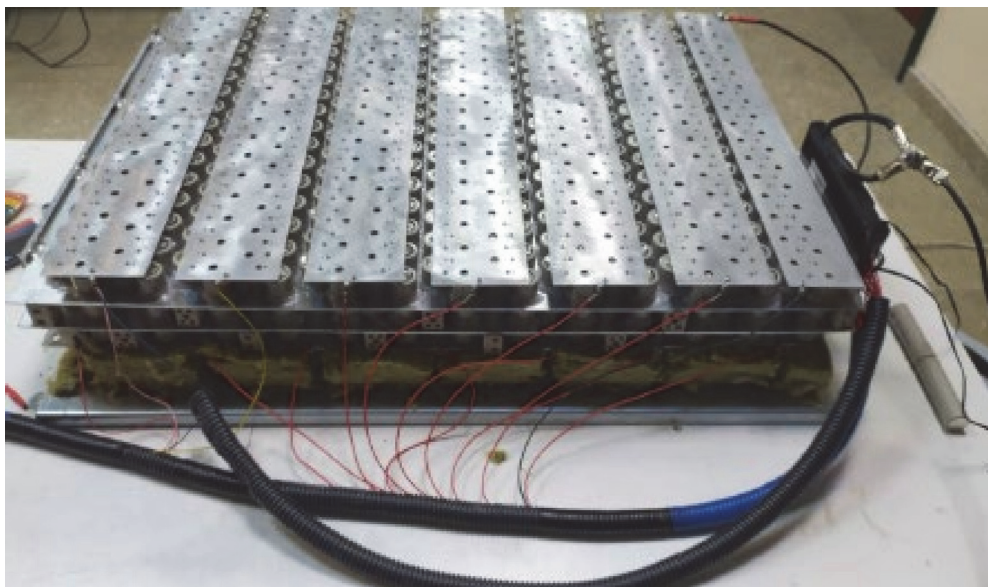
Figure 48. Connect battery pack with bms

As shown in Figure 48, the battery pack is combined with the BMS. The busbar seen in the top right corner is the negative terminal of the battery pack. In the bottom left corner, there is a positive terminal. BMS cables are fixed with a protective tube.

Figure 49. Battery Pack

The battery pack has been assembled with all its elements, and the assembly process has been completed. After activating the BMS, the voltages of each cell block were checked. And the voltages are 3.6V, 7.2V, 10.8V, 14.4V, 18V, 21.6V, 25.2V, 28.8V, 32.4V, 36V, 39.6V, 43.2 V, respectively. The voltage measured from the terminals is 43.2 volts. Warning signs regarding circuit breaker and battery pack occupational safety were affixed on the completed battery pack. A circuit breaker has been placed on the completed battery pack, apart from the BMS, in case of unexpected situations.

Figure 50. Drop test result for base plate

The battery pack, which was lifted to a height of 2 meters with a crane, was subjected to 2 tests: the base plate and edge tests. According to the base plate test results seen in Figure 50, no bending was observed on the outer surface of the package. The materials inside the package are not damaged.

As seen in Figure 51, no permanent deformation was observed in the edge test, and the inner material of the package was not damaged. Nevertheless, there are paint rips on the outer of the package.

Figure 51. Drop test result for edge

5.2.2. Thermal Result
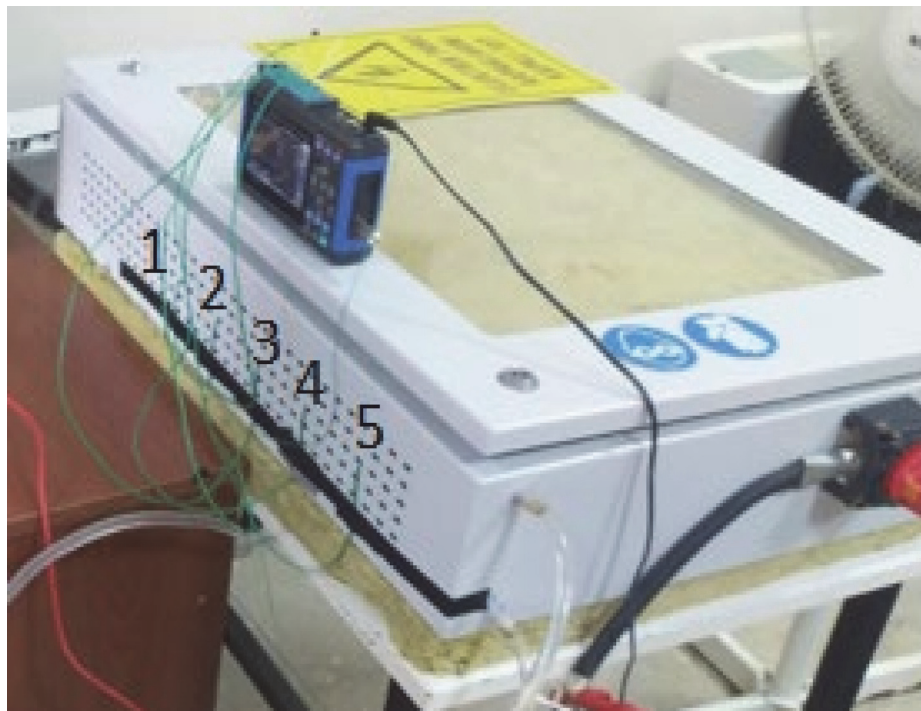
Figure 52. Thermocouple in air channel

As seen in the Figure 52, a thermocouple was placed in the air outlets on the battery pack. Voltage sensors were placed on the positive and negative terminals.
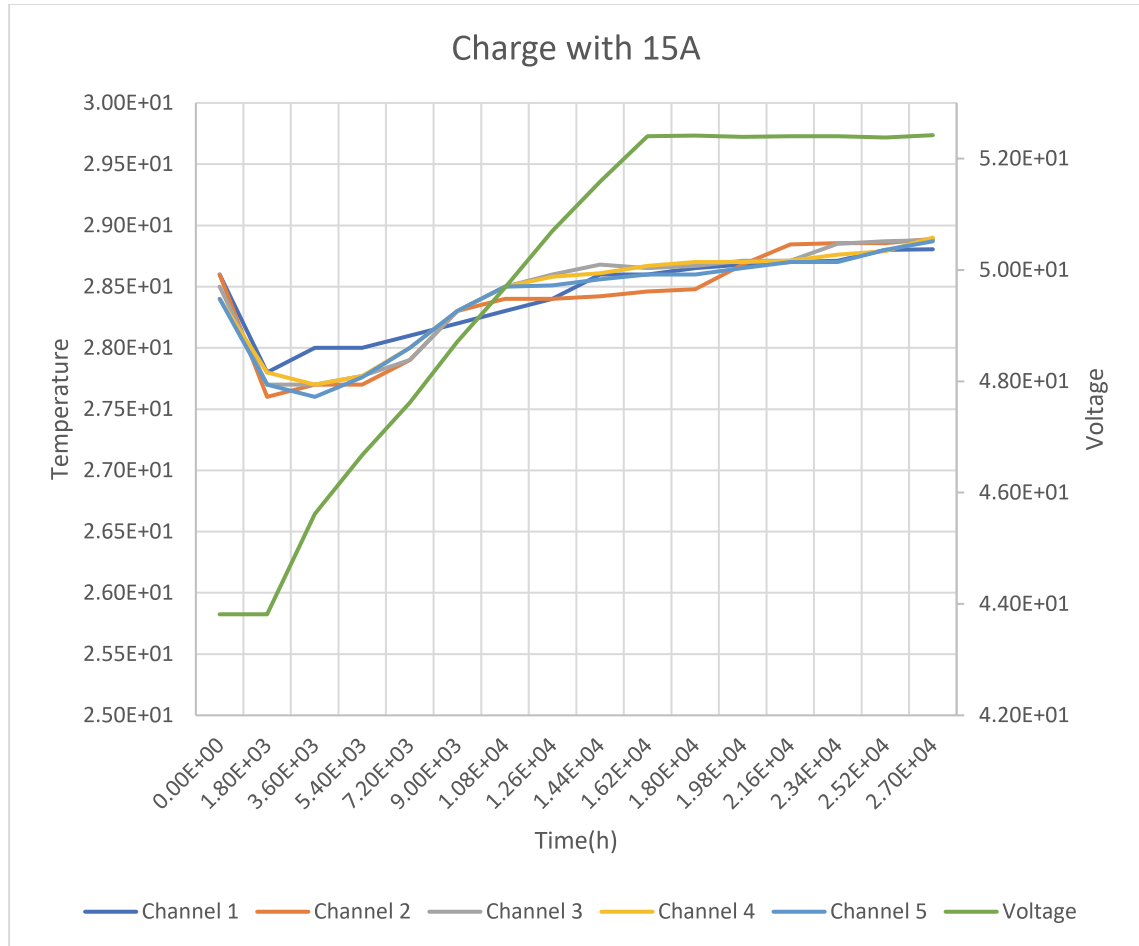
Figure 53. Temperature in 15A

The graph shows that charging was carried out with 15 amps for 7 hours. The ambient temperature in the charging process is 28.5 degrees. The circulator was set to 23 degrees. The air cooling rate is 2 m/s, and the liquid cooling flow rate is 0.1 kg/s. The fan and circulator were activated, and it was expected to stabilize for 30 minutes. The battery pack was then charged with 15 amps. As a result of the charging process, the temperature values in the channels gathered around 29 degrees.

The discharge process shown in the Figure 54 was reduced from 48 volts to 41 volts with 30 amps. The ambient temperature is 28 degrees, air velocity is 2m/s, and fluid flow is 0.1 kg/s. The maximum temperature value was observed at around 31 degrees during the discharge process.
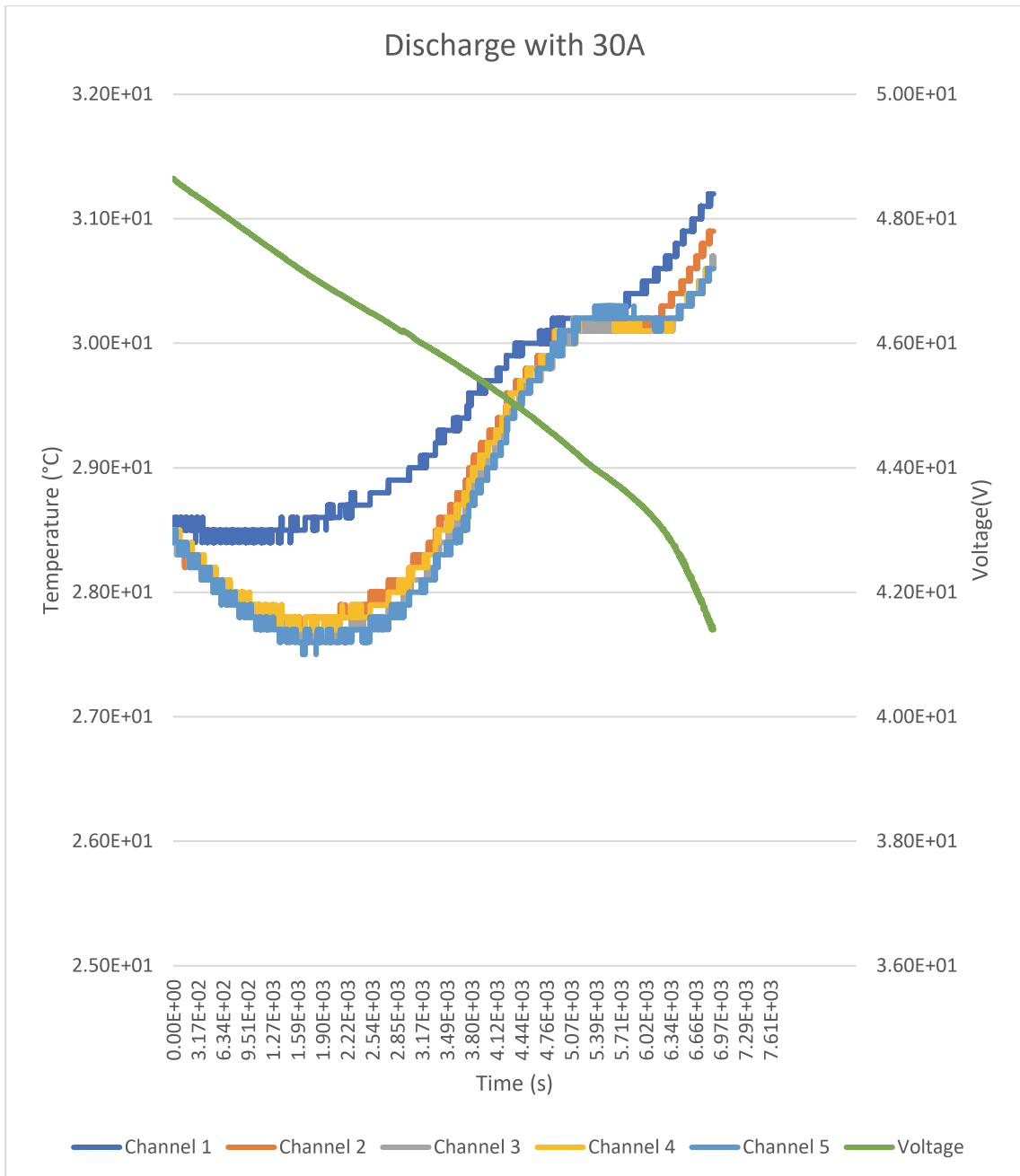
Figure 54. Temperature in 30A

The discharge process was carried out with a minimum of 0.2 A, and a maximum of 255A over the battery pack mounted on the electric vehicle. Battery pack temperatures reached 36 degrees , including ambient conditions. This maximum temperature value is also affected by the BMS temperature. BMS temperature reached a maximum of 91 degrees. Here it is necessary to consider cooling for the BMS.

Figure 55. BMS voltage and ampere result

Figure 56. Electric vehicle and battery pack

As seen in the Figure 56, the battery pack was mounted on the front of the electric vehicle. After 40 minutes of various driving tests, the battery charge level reduced from 94 % to 88 %.

CHAPTER 6

CONCLUSION

Today, companies such as Tesla, Toyota, and Chevrolet are trying to overcome thermal problems with their own designed battery pack thermal management systems in electric vehicles. For example, Tesla and Chevrolet have liquid-cooled vehicles, while Toyota has air-cooled models (Sanguesa et al. 2021). This project produces a battery pack with designs that provide optimum operating temperatures of the battery (including active and passive cooling methods).

Although there are many small-scale theoretical and experimental studies on battery packs, the number of theoretical and experimental studies for producing a 6.7 kWh battery pack is few. Classical heating/cooling methods and manifold designs in the literature are not sufficient as the size of the package increases. In this study, a 6.7 kWh battery pack was produced. Battery pack operation consists of 2 parts, mechanical and thermal. In the mechanical part, battery pack assembly and drop tests, one of the mechanical tests, were carried out. The battery pack was assembled using aluminum heat plate, aluminum cooling pipe, BMS, battery case, battery, and nickel strip. At the end of the battery pack assembly, voltage measurements were made, and the accuracy of the assembly was demonstrated. A numerical and experimental study supported drop tests. As a result of this study, the battery case did not show permanent deformation ($2.529x$ $108 N/m2$) as suggested in the numerical experiments ($1.263x$ $108 N/m2$). Discharge characteristics and battery module model were discussed in the thermal management part. The information in the literature confirmed the discharge characteristic. When the battery is discharged with 0.84A, 4.2A, 10A, 20A, and 30A, the discharge times are 17236.88s, 3522.02s, 1461.97s, 723.64s, 458.83s, respectively. The battery cell was simulated with the NTGK battery model to create a realistic model using the experimental data of the battery. The gap between the battery cells reached its most efficient value at 8 mm. At 8mm, the maximum temperature of the battery module was found to be 320K. In the developed battery module, thermal management was attempted using a heat plate and a cooling pipe. According to the numerical results, the battery module reaches 311.37K at 10C discharge. In the experimental process, the battery pack was charged with 15 amps

and discharged with 30 amps. Moreover, the temperature values reached a maximum of 31 degrees. In the experiment on electric vehicles, a maximum discharge level of 255 A was observed. In this experiment, the battery pack reached a maximum of 36 degrees.

REFERENCES

The Formability of Erdemir 6112 Sheet Metal by the Hydromechanical Deep
        Drawing Process." n.d. Accessed May 16, 2022.
        https://www.researchgate.net/publication/289348337_The_formability_of_erd
        emir_6112_sheet_metal_by_the_hydromechanical_deep_drawing_process.

"Thermal Evaluation of the Honda Insight Battery Pack." n.d.
        Accessed.May13,2022.https://www.researchgate.net/publication/241977847_
        Thermal_Evaluation_of_the_Honda_Insight_Battery_Pack.

"10.1115/IECEC2001-ET-07 ." 2013. Inactive DOIs, July.
        https://doi.org/10.1115/IECEC2001-ET-07.

Aluminum Electrical Conductor Handbook. 1989. 3rd ed. Washington D.C.: Aluminum
        Association.

"American Wire Gauge Chart and AWG Electrical Current Load Limits Table with
        Ampacities, Wire Sizes, Skin Depth Frequencies and Wire Breaking
        Strength." n.d. Accessed May 19, 2022.
        https://www.powerstream.com/Wire_Size.htm.

An, Zhoujian, Li Jia, Xuejiao Li, and Yong Ding. 2017. "Experimental Investigation on
        Lithium-Ion Battery Thermal Management Based on Flow Boiling in Mini-
        Channel." Applied Thermal Engineering 117 (May): 534–43.
        https://doi.org/10.1016/J.APPLTHERMALENG.2017.02.053.

Aneke, Mathew, and Meihong Wang. 2016. "Energy Storage Technologies and Real
        Life Applications – A State of the Art Review." Applied Energy 179
        (October): 350–77. https://doi.org/10.1016/J.APENERGY.2016.06.097.

"ANSYS Fluent Theory Guide." 2021. http://www.ansys.com.

Ashby, M. F. n.d. "Materials Selection in Mechanical Design," 646. Accessed May 29, 2022.

"AWG - American Wire Gauge Converting Chart." n.d. Accessed May 19, 2022. https://www.engineeringtoolbox.com/awg-wire-gauge-d_731.html.

Basu, Suman, Krishnan S. Hariharan, Subramanya Mayya Kolake, Taewon Song, Dong Kee Sohn, and Taejung Yeo. 2016. "Coupled Electrochemical Thermal Modelling of a Novel Li-Ion Battery Pack Thermal Management System." Applied Energy 181 (November): 1–13. https://doi.org/10.1016/J.APENERGY.2016.08.049.

Bejan, Adrian. 2013. "Convection Heat Transfer: Fourth Edition." Convection Heat Transfer: Fourth Edition, March. https://doi.org/10.1002/9781118671627.

Bobzin, K., M. Öte, M. A. Knoch, I. Alkhasli, and S. R. Dokhanchi. 2019. "Modelling of Particle Impact Using Modified Momentum Source Method in Thermal Spraying." IOP Conference Series: Materials Science and Engineering 480 (1). https://doi.org/10.1088/1757-899X/480/1/012003.

Chen, Kai, Yiming Chen, Zeyu Li, Fang Yuan, and Shuangfeng Wang. 2018. "Design of the Cell Spacings of Battery Pack in Parallel Air-Cooled Battery Thermal Management System." International Journal of Heat and Mass Transfer 127 (December): 393–401. https://doi.org/10.1016/J.IJHEATMASSTRANSFER.2018.06.131.

Chen, Kai, Mengxuan Song, Wei Wei, and Shuangfeng Wang. 2018. "Structure Optimization of Parallel Air-Cooled Battery Thermal Management System with U-Type Flow for Cooling Efficiency Improvement." Energy 145 (February): 603–13. https://doi.org/10.1016/J.ENERGY.2017.12.110.

Chen, Siqi, Xiongbin Peng, Nengsheng Bao, and Akhil Garg. 2019. "A Comprehensive Analysis and Optimization Process for an Integrated Liquid Cooling Plate for a Prismatic Lithium-Ion Battery Module." Applied Thermal Engineering 156

(June) : 324 – 39
https://doi.org/10.1016/J.APPLTHERMALENG.2019.04.089.

Coneybeer, Robert T., W. Z. Black, and R. A. Bush. 1994. "Steady-State and Transient
Ampacity of Bus Bar." IEEE Transactions on Power Delivery 9 (4): 1822–29.
https://doi.org/10.1109/61.329515.

Dan, Dan, Chengning Yao, Yangjun Zhang, Hu Zhang, Zezhi Zeng, and Xiaoming Xu.
2019. "Dynamic Thermal Behavior of Micro Heat Pipe Array-Air Cooling
Battery Thermal Management System Based on Thermal Network Model."
Applied Thermal Engineering 162 (November): 114183.
https://doi.org/10.1016/J.APPLTHERMALENG.2019.114183.

Das, Abhishek, Anup Barai, Iain Masters, and David Williams. 2019. "Comparison of
Tab-To-Busbar Ultrasonic Joints for Electric Vehicle Li-Ion Battery
Applications." World Electric Vehicle Journal 2019, Vol. 10, Page 55 10 (3):
55. https://doi.org/10.3390/WEVJ10030055.

Deng, Tao, Guodong Zhang, Yan Ran, and Ping Liu. 2019. "Thermal Performance of
Lithium Ion Battery Pack by Using Cold Plate." Applied Thermal Engineering
160 (September): 114088.
https://doi.org/10.1016/J.APPLTHERMALENG.2019.114088.

"Drop Test Studies - 2020 - SOLIDWORKS Help." n.d. Accessed May 16, 2022.
https://help.solidworks.com/2020/english/SolidWorks/cworks/c_Drop_Test_St
udies.htm.

Du, Jiuyu, Yizhao Sun, Yingxuan Huang, and Xiaogang Wu. 2020. "Analysis of
Influencing Factors of Thermal Management System for LiFePO4 Lithium
Battery under High Power Charging." World Electric Vehicle Journal 2020,
Vol. 11, Page 44 11 (2): 44. https://doi.org/10.3390/WEVJ11020044.

Fan, Yuqian, Yun Bao, Chen Ling, Yanyan Chu, Xiaojun Tan, and Shuting Yang. 2019.
    "Experimental Study on the Thermal Management Performance of Air
    Cooling for High Energy Density Cylindrical Lithium-Ion Batteries." Applied
    Thermal Engineering 155 (June): 96–109.
    https://doi.org/10.1016/J.APPLTHERMALENG.2019.03.157.

Feng, Xuning, Minggao Ouyang, Xiang Liu, Languang Lu, Yong Xia, and Xiangming
    He. 2018. "Thermal Runaway Mechanism of Lithium Ion Battery for Electric
    Vehicles: A Review." Energy Storage Materials 10 (January): 246–67.
    https://doi.org/10.1016/J.ENSM.2017.05.013.

Fu-qiang, AN, ZHAO Hong-liang, CHENG Zhi, QIU JI Yi-cheng, ZHOU Wei-nan, LI
    Ping, AN Fu-qiang, et al. 2019. "Development Status and Research Progress
    of Power Battery for Pure Electric Vehicles." Chinese Journal of Engineering,
    2019, Vol. 41, Issue 1, Pages: 22-42 41 (1): 22–42.
    https://doi.org/10.13374/J.ISSN2095-9389.2019.01.003.

"Generic Battery Model - Simulink." n.d. Accessed May 13, 2022a.
    https://www.mathworks.com/help/physmod/sps/powersys/ref/battery.html.

"Generic Battery Model - Simulink." . n.d. Accessed May 13, 2022b.
    https://www.mathworks.com/help/physmod/sps/powersys/ref/battery.html.

Gocmen, Sinan, and Erdal Cetkin. 2022. "Emergence of Elevated Battery Positioning in
    Air Cooled Battery Packs for Temperature Uniformity in Ultra-Fast
    Dis/Charging Applications." Journal of Energy Storage 45 (January): 103516.
    https://doi.org/10.1016/J.EST.2021.103516.

Gungor, Sahin, Erdal Cetkin, and Sylvie Lorente. 2022a. "Canopy-to-Canopy Liquid
    Cooling for the Thermal Management of Lithium-Ion Batteries, a Constructal
    Approach." International Journal of Heat and Mass Transfer 182 (January):
    121918. https://doi.org/10.1016/J.IJHEATMASSTRANSFER.2021.121918.

2022b. "Thermal and Electrical Characterization of an Electric Vehicle Battery Cell, an Experimental Investigation." Applied Thermal Engineering 212 (July): 118530. https://doi.org/10.1016/J.APPLTHERMALENG.2022.118530.

Huang, C. -K., J. S. Sakamoto, J. Wolfenstine, and S. Surampudi. 2000. "The Limits of Low-Temperature Performance of Li-Ion Cells." Journal of The Electrochemical Society 147 (8): 2893. https://doi.org/10.1149/1.1393622.

Huang, Yuqi, Pan Mei, Yiji Lu, Rui Huang, Xiaoli Yu, Zhuolie Chen, and Anthony Paul Roskilly. 2019. "A Novel Approach for Lithium-Ion Battery Thermal Management with Streamline Shape Mini Channel Cooling Plates." Applied Thermal Engineering 157 (July): 113623. https://doi.org/10.1016/J.APPLTHERMALENG.2019.04.033.

"INR-21700-P42A – Molicel." n.d. Accessed May 13, 2022. https://www.molicel.com/product/inr-21700-p42a/.

Jacob, Paul., Lee. Goulding, and National Agency for Finite Element Methods & Standards (Great Britain). 2002. An Explicit Finite Element Primer. Glasgow: NAFEMS.

Jaguemont, J., L. Boulon, and Y. Dubé. 2016. "A Comprehensive Review of Lithium-Ion Batteries Used in Hybrid and Electric Vehicles at Cold Temperatures." Applied Energy 164 (February): 99–114. https://doi.org/10.1016/J.APENERGY.2015.11.034.

Ji, Changwei, Bing Wang, Shuofeng Wang, Shuai Pan, Du Wang, Pengfei Qi, and Kai Zhang. 2019. "Optimization on Uniformity of Lithium-Ion Cylindrical Battery Module by Different Arrangement Strategy." Applied Thermal Engineering 157 (July): 113683. https://doi.org/10.1016/J.APPLTHERMALENG.2019.04.093.

Jiaqiang, E., Meng Yue, Jingwei Chen, Hao Zhu, Yuanwang Deng, Yun Zhu, Feng Zhang, Ming Wen, Bin Zhang, and Siyi Kang. 2018. "Effects of the Different Air Cooling Strategies on Cooling Performance of a Lithium-Ion Battery Module with Baffle." Applied Thermal Engineering 144 (November): 231–41. https://doi.org/10.1016/J.APPLTHERMALENG.2018.08.064.

Kirad, Kumar, and Mangesh Chaudhari. 2021. "Design of Cell Spacing in Lithium-Ion Battery Module for Improvement in Cooling Performance of the Battery Thermal Management System." Journal of Power Sources 481 (January): 229016. https://doi.org/10.1016/J.JPOWSOUR.2020.229016.

Li, Wei, Mi Xiao, Xiongbin Peng, Akhil Garg, and Liang Gao. 2019. "A Surrogate Thermal Modeling and Parametric Optimization of Battery Pack with Air Cooling for EVs." Applied Thermal Engineering 147 (January): 90–100. https://doi.org/10.1016/J.APPLTHERMALENG.2018.10.060.

Li, Xinxi, Fengqi He, Guoqing Zhang, Qiqiu Huang, and Dequan Zhou. 2019. "Experiment and Simulation for Pouch Battery with Silica Cooling Plates and Copper Mesh Based Air Cooling Thermal Management System." Applied Thermal Engineering 146 (January): 866–80. https://doi.org/10.1016/J.APPLTHERMALENG.2018.10.061.

Li, Xinxi, Qiqiu Huang, Jian Deng, Guoqing Zhang, Zhaoda Zhong, and Fengqi He. 2020. "Evaluation of Lithium Battery Thermal Management Using Sealant Made of Boron Nitride and Silicone." Journal of Power Sources 451 (March): 227820. https://doi.org/10.1016/J.JPOWSOUR.2020.227820.

Li, Yubai, Zhifu Zhou, and Wei Tao Wu. 2019. "Three-Dimensional Thermal Modeling of Li-Ion Battery Cell and 50 V Li-Ion Battery Pack Cooled by Mini-Channel Cold Plate." Applied Thermal Engineering 147 (January): 829–40. https://doi.org/10.1016/J.APPLTHERMALENG.2018.11.009.

Ling, Ziye, Fangxian Wang, Xiaoming Fang, Xuenong Gao, and Zhengguo Zhang.
2015. "A Hybrid Thermal Management System for Lithium Ion Batteries
Combining Phase Change Materials with Forced-Air Cooling." Applied
Energy 148 (June): 403–9.
https://doi.org/10.1016/J.APENERGY.2015.03.080.

Liu, Zhengyu, Hao Wang, Chao Yang, and Jingjie Zhao. 2020. "Simulation Study of
Lithium-Ion Battery Thermal Management System Based on a Variable Flow
Velocity Method with Liquid Metal." Applied Thermal Engineering 179
(October): 115578.
https://doi.org/10.1016/J.APPLTHERMALENG.2020.115578.

Lu, Zhao, Xiaoling Yu, Lichuan Wei, Yalin Qiu, Liyu Zhang, Xiangzhao Meng, and
Liwen Jin. 2018. "Parametric Study of Forced Air Cooling Strategy for
Lithium-Ion Battery Pack with Staggered Arrangement." Applied Thermal
Engineering 136 (May): 28–40.
https://doi.org/10.1016/J.APPLTHERMALENG.2018.02.080.

Lv, Youfu, Dequan Zhou, Xiaoqing Yang, Xiangyun Liu, Xinxi Li, and Guoqing
Zhang. 2019. "Experimental Investigation on a Novel Liquid-Cooling Strategy
by Coupling with Graphene-Modified Silica Gel for the Thermal Management
of Cylindrical Battery." Applied Thermal Engineering 159 (August): 113885.
https://doi.org/10.1016/J.APPLTHERMALENG.2019.113885.

Menale, Carla, Francesco D'Annibale, Barbara Mazzarotta, and Roberto Bubbico. 2019.
"Thermal Management of Lithium-Ion Batteries: An Experimental
Investigation." Energy 182 (September): 57–71.
https://doi.org/10.1016/J.ENERGY.2019.06.017.

Miele, Amy, Jonn Axsen, Michael Wolinetz, Elicia Maine, and Zoe Long. 2020. "The
Role of Charging and Refuelling Infrastructure in Supporting Zero-Emission
Vehicle Sales." Transportation Research Part D: Transport and Environment
81 (April): 102275. https://doi.org/10.1016/J.TRD.2020.102275.

Mossali, Elena, Nicoletta Picone, Luca Gentilini, Olga Rodrìguez, Juan Manuel Pérez, and Marcello Colledani. 2020. "Lithium-Ion Batteries towards Circular Economy: A Literature Review of Opportunities and Issues of Recycling Treatments." Journal of Environmental Management 264 (June): 110500. https://doi.org/10.1016/J.JENVMAN.2020.110500.

Nitta, N, F Wu, JT Lee, G Yushin - Materials today, and undefined 2015. n.d. "Li-Ion Battery Materials: Present and Future." Elsevier. Accessed May 13, 2022. https://www.sciencedirect.com/science/article/pii/S1369702114004118.

Panchal, S., R. Khasow, I. Dincer, M. Agelin-Chaab, R. Fraser, and M. Fowler. 2017. "Thermal Design and Simulation of Mini-Channel Cold Plate for Water Cooled Large Sized Prismatic Lithium-Ion Battery." Applied Thermal Engineering 122 (July): 80–90. https://doi.org/10.1016/J.APPLTHERMALENG.2017.05.010.

Peng, Xiongbin, Chong Ma, Akhil Garg, Nengsheng Bao, and Xiangping Liao. 2019. "Thermal Performance Investigation of an Air-Cooled Lithium-Ion Battery Pack Considering the Inconsistency of Battery Cells." Applied Thermal Engineering 153 (May): 596–603. https://doi.org/10.1016/J.APPLTHERMALENG.2019.03.042.

Rao, Zhonghao, Zhen Qian, Yong Kuang, and Yimin Li. 2017. "Thermal Performance of Liquid Cooling Based Thermal Management System for Cylindrical Lithium-Ion Battery Module with Variable Contact Surface." Applied Thermal Engineering 123 (August): 1514–22. https://doi.org/10.1016/J.APPLTHERMALENG.2017.06.059.

Rezvani, Zeinab, Johan Jansson, and Jan Bodin. 2015. "Advances in Consumer Electric Vehicle Adoption Research: A Review and Research Agenda." Transportation Research Part D: Transport and Environment 34 (January): 122–36. https://doi.org/10.1016/J.TRD.2014.10.010.

Roe, Charlotte, Xuning Feng, Gavin White, Ruihe Li, Huaibin Wang, Xinyu Rui, Cheng
    Li, et al. 2022. "Immersion Cooling for Lithium-Ion Batteries – A Review."
    Journal of Power Sources 525 (March): 231094.
    https://doi.org/10.1016/J.JPOWSOUR.2022.231094.

"Safe Drop Test Measurements for HV Electric Vehicle Batteries | CSM GmbH." n.d.
    Accessed May 16, 2022. https://www.csm.de/en/fields-of-application/use-
    cases/high-voltage-measurement-of-analog-voltages/1050-safe-drop-test-
    measurements-for-hv-electric-vehicle-
    batteries?highlight=WyJzdGFuZGFyZCJd.

Sanguesa, Julio A., Vicente Torres-Sanz, Piedad Garrido, Francisco J. Martinez, and
    Johann M. Marquez-Barja. 2021. "A Review on Electric Vehicles:
    Technologies and Challenges." Smart Cities 2021, Vol. 4, Pages 372-404 4
    (1): 372–404. https://doi.org/10.3390/SMARTCITIES4010022.

Santos, Georgina. 2017. "Road Transport and CO2 Emissions: What Are the
    Challenges?" Transport Policy 59 (October): 71–74.
    https://doi.org/10.1016/J.TRANPOL.2017.06.007.

Shang, Zhuangzhuang, Hongzhong Qi, Xintian Liu, Chenzhi Ouyang, and Yansong
    Wang. 2019. "Structural Optimization of Lithium-Ion Battery for Improving
    Thermal Performance Based on a Liquid Cooling System." International
    Journal of Heat and Mass Transfer 130 (March): 33–41.
    https://doi.org/10.1016/J.IJHEATMASSTRANSFER.2018.10.074.

Sharma, Dinesh Kumar, and Aneesh Prabhakar. 2021. "A Review on Air Cooled and
    Air Centric Hybrid Thermal Management Techniques for Li-Ion Battery Packs
    in Electric Vehicles." Journal of Energy Storage 41 (September): 102885.
    https://doi.org/10.1016/J.EST.2021.102885.

Shen, Ming, and Qing Gao. 2020. "System Simulation on Refrigerant-Based Battery
       Thermal Management Technology for Electric Vehicles." Energy Conversion
       and Management 203 (January): 112176.
       https://doi.org/10.1016/J.ENCONMAN.2019.112176.

Sun, Peiyi, Roeland Bisschop, Huichang Niu, and Xinyan Huang. 2020. "A Review of
       Battery Fires in Electric Vehicles." Fire Technology 2020 56:4 56 (4): 1361–
       1410. https://doi.org/10.1007/S10694-019-00944-3.

"Test of Molicel INR21700-P42A 4200mAh (Gray)." n.d. Accessed May 16, 2022.
       https://lygte-info.dk/review/batteries2012/Molicel%20INR21700-
       P42A%204200mAh%20(Gray)%20UK.html.

"The Global Electric Car Sales 2021 in Numbers - JATO." n.d. Accessed May 13, 2022.
       https://www.jato.com/the-global-electric-car-sales-2021-in-numbers/.

Thøgersen, John, and Jonas v. Ebsen. 2019. "Perceptual and Motivational Reasons for
       the Low Adoption of Electric Cars in Denmark." Transportation Research Part
       F: Traffic Psychology and Behaviour 65 (August): 89–106.
       https://doi.org/10.1016/J.TRF.2019.07.017.

Tran, Thanh Ha, Souad Harmand, Bernard Desmet, and Sebastien Filangi. 2014.
       "Experimental Investigation on the Feasibility of Heat Pipe Cooling for
       HEV/EV Lithium-Ion Battery." Applied Thermal Engineering 63 (2): 551–58.
       https://doi.org/10.1016/J.APPLTHERMALENG.2013.11.048.

"Understanding the Neher-McGrath Calculation and the Ampacity of Conductors." n.d.
       Accessed May 19, 2022. http://www.electrician2.com/articles/ampacity.htm.

Wang, Q., B. Jiang, Q. F. Xue, H. L. Sun, B. Li, H. M. Zou, and Y. Y. Yan. 2015.
       "Experimental Investigation on EV Battery Cooling and Heating by Heat
       Pipes." Applied Thermal Engineering 88 (September): 54–60.
       https://doi.org/10.1016/J.APPLTHERMALENG.2014.09.083.

Wang, Tao, K. J. Tseng, Jiyun Zhao, and Zhongbao Wei. 2014. "Thermal Investigation
of Lithium-Ion Battery Module with Different Cell Arrangement Structures
and Forced Air-Cooling Strategies." Applied Energy 134 (December): 229–38.
https://doi.org/10.1016/J.APENERGY.2014.08.013.

Wang, Yan, Qing Gao, Guohua Wang, Pengyu Lu, Mengdi Zhao, and Wendi Bao.
2018. "A Review on Research Status and Key Technologies of Battery
Thermal Management and Its Enhanced Safety." International Journal of
Energy Research 42 (13): 4008–33. https://doi.org/10.1002/ER.4158.

Xu, Xinhai, Wenzheng Li, Ben Xu, and Jiang Qin. 2019. "Numerical Study on a Water
Cooling System for Prismatic LiFePO4 Batteries at Abused Operating
Conditions." Applied Energy 250 (September): 404–12.
https://doi.org/10.1016/J.APENERGY.2019.04.180.

Yang, Wen, Fei Zhou, Haobing Zhou, Qianzhi Wang, and Jizhou Kong. 2020. "Thermal
Performance of Cylindrical Lithium-Ion Battery Thermal Management System
Integrated with Mini-Channel Liquid Cooling and Air Cooling." Applied
Thermal Engineering 175 (July): 115331.
https://doi.org/10.1016/J.APPLTHERMALENG.2020.115331.

Yates, Matthew, Mohammad Akrami, and Akbar A. Javadi. 2021. "Analysing the
Performance of Liquid Cooling Designs in Cylindrical Lithium-Ion Batteries."
Journal of Energy Storage 33 (January): 100913.
https://doi.org/10.1016/J.EST.2019.100913.

Ye, Xin, Yaohua Zhao, and Zhenhua Quan. 2018. "Experimental Study on Heat
Dissipation for Lithium-Ion Battery Based on Micro Heat Pipe Array
(MHPA)." Applied Thermal Engineering 130 (February): 74–82.
https://doi.org/10.1016/J.APPLTHERMALENG.2017.10.141.

Ye, Yonghuang, Lip Huat Saw, Yixiang Shi, and Andrew A.O. Tay. 2015. "Numerical
        Analyses on Optimizing a Heat Pipe Thermal Management System for
        Lithium-Ion Batteries during Fast Charging." Applied Thermal Engineering 86
        (July): 281–91. https://doi.org/10.1016/J.APPLTHERMALENG.2015.04.066.

Ye, Yonghuang, Yixiang Shi, Lip Huat Saw, and Andrew A.O. Tay. 2016.
        "Performance Assessment and Optimization of a Heat Pipe Thermal
        Management System for Fast Charging Lithium Ion Battery Packs."
        International Journal of Heat and Mass Transfer 92 (January): 893–903.
        https://doi.org/10.1016/J.IJHEATMASSTRANSFER.2015.09.052.

Young, Warren C., Richard G Budynas, and Ali Sadegh. 2012. "Roark's Formulas for
        Stress and Strain, 8th Edition," 1072. http://www.amazon.co.uk/Roarks-
        Formulas-Stress-Strain-Edition/dp/0071742476.

Yu, Kuahai, Xi Yang, Yongzhou Cheng, and Changhao Li. 2014. "Thermal Analysis
        and Two-Directional Air Flow Thermal Management for Lithium-Ion Battery
        Pack." Journal of Power Sources 270 (December): 193–200.
        https://doi.org/10.1016/J.JPOWSOUR.2014.07.086.

Zhang, Xiongwen, Xin Kong, Guojun Li, and Jun Li. 2014. "Thermodynamic
        Assessment of Active Cooling/Heating Methods for Lithium-Ion Batteries of
        Electric Vehicles in Extreme Conditions." Energy 64 (January): 1092–1101.
        https://doi.org/10.1016/J.ENERGY.2013.10.088.

Zhao, Gang, Xiaolin Wang, and Michael Negnevitsky. 2022. "Connecting Battery
        Technologies for Electric Vehicles from Battery Materials to Management."
        IScience 25 (2): 103744. https://doi.org/10.1016/J.ISCI.2022.103744.

Zhao, Rui, Junjie Gu, and Jie Liu. 2015. "An Experimental Study of Heat Pipe Thermal
        Management System with Wet Cooling Method for Lithium Ion Batteries."
        Journal of Power Sources 273 (January): 1089–97.
        https://doi.org/10.1016/J.JPOWSOUR.2014.10.007.

Zhou, Haobing, Fei Zhou, Lipeng Xu, Jizhou Kong, and QingxinYang. 2019. "Thermal
  Performance of Cylindrical Lithium-Ion Battery Thermal Management System
  Based on Air Distribution Pipe." International Journal of Heat and Mass
  Transfer 131 (March): 984–98.
  https://doi.org/10.1016/J.IJHEATMASSTRANSFER.2018.11.116.

Zhou, Haobing, Fei Zhou, Qian Zhang, Qianzhi Wang, and Zebin Song. 2019. "Thermal
  Management of Cylindrical Lithium-Ion Battery Based on a Liquid Cooling
  Method with Half-Helical Duct." Applied Thermal Engineering 162
  (November): 114257.
  https://doi.org/10.1016/J.APPLTHERMALENG.2019.114257.

Zolot, Matthew, Ahmad A. Pesaran, and Mark Mihalic. 2002. "Thermal Evaluation of
  Toyota Prius Battery Pack." SAE Technical Papers.
  https://doi.org/10.4271/2002-01-1962.

Zwicker, M. F.R., M. Moghadam, W. Zhang, and C. v. Nielsen. 2020. "Automotive
  Battery Pack Manufacturing – a Review of Battery to Tab Joining." Journal of
  Advanced Joining Processes 1 (March): 100017.
  https://doi.org/10.1016/J.JAJP.2020.100017.